TAMPEREEN TEKNILLINEN YLIOPISTO
TAMPERE UNIVERSITY OF TECHNOLOGY

JUUSO HEIKKINEN

NOVEL STRAIN FIELD IMAGING USING ELECTRONIC SPECKLE PATTERN INTERFEROMETRY

Master's thesis

Examiner: Associate Professor Juha Toivonen
The examiner and topic of the thesis were approved by the Council of the Faculty of Natural Sciences on 4 May 2016

ABSTRACT

TAMPERE UNIVERSITY OF TECHNOLOGY
Master's Programme in Science and Engineering
JUUSO HEIKKINEN: Novel Strain Field Imaging Using Electronic Speckle Pattern Interferometry
Master of Science Thesis, 58 pages
June 2016
Major: Advanced Engineering Physics
Examiner: Associate Professor Juha Toivonen
Keywords: ESPI, strain, phasor, filtering, laser, coherence, diffraction grating

Growing demands for cost and energy efficiency set requirements for developing lighter and stronger products. The strength of material is characterized by maximum tolerable stress. For a given material, stress is directly related to strain, and strain measurement provides a practical way for estimating mechanical strength. Traditional strain gauges are simple and very robust, but their use is limited, since the measurements are taken at only discrete locations; long setup times are required; and maximum strain resolution is limited.

Electronic speckle pattern interferometry (ESPI) is a very sensitive optical method for measuring full field displacements on the surface of a test object. Strain field is obtained by numerically differentiating the displacement field. Full field recording makes ESPI practical for quality control applications, since material faults cause strain concentrations that would be impractical or even impossible to detect using strain gauges. However, ESPI recordings contain noise that is amplified by the differentiation process. In the presence of large strains the noise level further rises due to increasing speckle decorrelation effect. Hence, the strain measurement range is ultimately limited by the ability to successfully filter out measurement noise.

In this thesis, a filtering algorithm was developed to obtain good performance in the presence of large strains. In the algorithm, the measured displacement field is first repetitively mean filtered. The strain field is then calculated from the filtered displacement field. Amplified residual noise is removed by repetitively filtering the calculated strain field. Unlike in existing methods, data is handled in phasor format. This removes the need to unwrap the data, which often is the most critical and time-consuming step. In addition, the repetitive mean filtering is computationally simple and essentially self-adaptive. Compared to existing ESPI filtering methods, the developed algorithm achieves comparable or better performance but is also significantly faster. This enables real time monitoring of the strain field.

As a second objective, a novel measurement setup was developed. Current ESPI systems require high-coherence lasers that tend to be costly and bulky. In this thesis, a compact and affordable laser diode was used in combination with a reflection diffraction grating. The grating relaxes coherence requirements so that even a low-coherence laser diode can be applied. The novel measurement setup shows promising performance but the obtained strain resolution is slightly lower than that of high-coherence ESPI. It is expected that with small hardware improvements the laser diode based ESPI can narrow the gap to the high-coherence ESPI.

TIIVISTELMÄ

TAMPEREEN TEKNILLINEN YLIOPISTO
Teknis-luonnontieteellinen koulutusohjelma
JUUSO HEIKKINEN: Venymäkentän kuvantaminen käyttäen elektronista täpläkuviointerferometriaa
Diplomityö, 58 sivua
Kesäkuu 2016
Pääaine: Teknillinen fysiikka
Tarkastaja: Associate Professor Juha Toivonen
Avainsanat: ESPI, venymä, vektoriformatoitu, suodatus, laser, koherenssi, diffraktiohila

Kasvavat kustannus- ja energiatehokkuusvaatimukset edellyttävät kevyempien ja lujempien tuotteiden kehittämistä. Materiaalin lujuutta kuvaa sen kestämä maksimijännitys. Materiaalikohtaisesti jännitys on suoraan verrannollinen venymään, joten venymämittaus tarjoaa käytännöllisen tavan mekaanisen kestävyyden arvioimiseen. Perinteiset venymäliuskat ovat vakaita ja yksinkertaisia, mutta niiden sovellettavuus rajoitettua: mittauksia voidaan tehdä vain yksittäisissä kohdissa, valmisteluajat pitkiä ja venymän mittausresoluutio rajoitettu.

Elektroninen täpläkuviointerferometria (electronic speckle pattern interferometry, ESPI) on erittäin herkkä optinen mittamenetelmä, jolla voidaan mitata koko tutkittavan kappaleen pinnan siirtymäkenttä. Venymäkenttä saadaan siirtymäkentästä numeerisella derivoinnilla. Kuvamuotoinen mittadata tekee ESPI:stä käytännöllisen laadunvalvontasovelluksiin, sillä materiaalivauriot aiheuttavat venymäkonsentraatioita, joita olisi epäkäytännöllistä tai jopa mahdotonta havaita venymäliuskoilla. Toisaalta, ESPI-mittadatassa on kohinaa, jota numeerinen derivointi vahvistaa. Suuret venymät saavat aikaan kohinatason kasvun johtuen täplädekorrelaatioilmiöstä. Kohinansuodatuksen laatu vaikuttaa suoraan saavutettavaan venymäresoluutioon.

Tässä diplomityössä kehitettiin kohinansuodatusalgoritmi, jonka päätavoite oli saavuttaa hyvä toimintakyky suurilla venymätasoilla. Aluksi mitattu siirtymäkenttä suodatetaan käyttäen toistettavaa keskiarvosuodatinta. Venymäkenttä lasketaan suodatetusta siirtymäkentästä. Jäännöskohina suodatetaan pois venymäkentästä vastaavalla tavalla käyttäen toistettavaa keskiarvosuodatusta. Toisin kuin olemassa olevissa menetelmissä, data käsitellään vektoriformaatissa. Näin voidaan välttää datan purkaminen (unwrapping), joka usein on kriittisin ja hitain vaihe. Kehitetty algoritmi on laskennallisesti yksinkertainen ja automaattisesti mukautuva. Verrattuna olemassa oleviin ESPI-suodatusmenetelmiin, kehitetyn algoritmin suorituskyky on vastaava tai jopa parempi, mutta algoritmi on lisäksi huomattavasti nopeampi. Nopea prosessointi mahdollistaa jopa reaaliaikaisen venymäkentän monitoroinnin.

Toisena tavoitteena kehitettiin uudenlainen mittauslaitteisto. Nykyiset ESPI-laitteistot vaativat korkean koherenssin lasereita, jotka ovat kookkaita ja kalliita. Tässä diplomityössä käytettiin kompaktia ja edullista laserdiodia yhdessä heijastustyyppisen diffraktiohilan kanssa. Hila lieventää koherenssivaatimuksia siten, että jopa matalan koherenssin laserdiodia voidaan käyttää. Kehitetty laitteisto toimii lupaavasti, mutta saavutettu venymäresoluutio on hieman alhaisempi kuin korkean koherenssin ESPI-laitteistoilla. Pienillä laitteistoparannuksilla ero voidaan oletettavasti kuroa umpeen.

PREFACE

The research for this Master's thesis was conducted in the Renewable Resources Laboratory at the University of British Columbia, Vancouver, Canada. The thesis was funded by Stresstech Oy, and a travel grant was provided by Tampere University of Technology. I would like to express my deepest gratitude to Professor Gary Schajer for supervising this thesis, for many valuable discussions, and for continuous encouragement. I would like to thank Associate Professor Juha Toivonen for thesis examination and feedback; Stresstech Oy CEO Lasse Suominen for arranging the thesis position and funding; and UBC labmates for the fun times in and outside of the laboratory. Lastly, I want to thank my family and friends for their endless support and care.

The strain calculation algorithm developed in this thesis and some of the relating results will be sent for publication in The Conference Proceedings of the Society for Experimental Mechanics Series.

In Jyväskylä, Finland, on 15 June 2016

Juuso Heikkinen

TABLE OF CONTENTS

ABBREVIATIONS AND SYMBOLS

DIC	digital image correlation
DPSS	diode-pumped solid-state
ESPI	electronic speckle pattern interferometry
FEM	Finite element method
FOV	field of view
MRI	magnetic resonance imaging
LPA	local polynomial approximation
OPD	optical path difference
OPL	optical path length
PZT	piezoelectric transducer
SNR	signal-to-noise ratio
TV	total-variation

D	diameter of the collimated laser beam
$\boldsymbol{d}$	deformation vector
d	path length
d_g	groove separation
d_i	image distance
d_l	diameter of the imaging lens
d_o	object distance
E_{AB}	Complex strain component AB
f	focal length
$f\#$	lens f-number
I_j	intensity of wave j
I_{avg}	average intensity
I_{mod}	modulation intensity
I_S	intensity of an interference wave
$\boldsymbol{k_1}$	illumination vector 1
$\boldsymbol{k_2}$	illumination vector 2
$\boldsymbol{k_o}$	observation vector
$\boldsymbol{K_s}$	sensitivity vector
l_c	coherence length
l_i	coherence interval
L_{ij}	separation of pixels i and j
M	magnification ratio
m	diffraction order
n	refractive index
S	size of subjective speckles
V	visibility
θ_{i}	angle i
ε_{AB}	strain component AB
λ	wavelength
γ	groove angle
Φ	complex phase difference
ϕ	phase difference

1. INTRODUCTION

Determination of the structural strength of components and devices is crucial for a wide range of applications. It is important to verify that products can safely handle the loads they are designed for, and to monitor against potential material faults. Manufacturing industry benefits from quality control methods for monitoring component variations in order to keep process tolerances low. In addition, increasingly valued cost and energy efficiency set demands for developing lighter and stronger components.

The strength of a material is characterised by the maximum stress it can handle. Stress represents the internal forces per unit area in a material due to externally applied forces. Strain, on the other hand, is the change of length per unit length, and represents the degree of deformation. Stress-strain relationship is a material-specific characteristic. Under small loads, the relation between the applied load and the resulting deformation remains constant [1], a relation known as Hooke's Law. Because strain can be measured directly, it provides an easy and practical way to assess the strength of materials.

1.1 From strain gauges to optical strain measurement methods

Strain gauges have traditionally been used for measuring strains in various components. In the last decades, however, optical methods have become more popular and replaced strain gauges in many applications.

A strain gauge is physically attached on the surface of a test object. The deformation of the test object changes the length and thus the electrical resistance of a strain gauge. When calibrated, strain gauges can be used for strain measurements at very high accuracy. Strain gauges measure the average strain between the attachment points of gauge elements [2]. Hence, the measurement is dependent on the length and orientation of the gauge. Average-type measurement restricts the capability to detect the location of and measure the amplitude of very high strain concentrations. Because strains in test objects are rarely uniform, great care has to be used when choosing measurement directions and locations. Specific strain gauge arrangements have been developed to standardize measurements and to ensure that all strain components can be measured and stress components calculated [3, 4].

The main advantage of strain gauges is their high accuracy and robustness. The physical attachment avoids artifacts due to rigid body motions. In general strain gauges are much less prone to noise than optical methods. However, strain gauges provide only average

strain and over a small area of the test specimen. The observation of high gradients and material faults is difficult. In addition, the required physical contact can affect the measurement. Strain gauges are not re-usable and the contact may damage the object surface. Each gauge has to be separately glued to the object surface, so significant preparation time is required. Electrical resistivity is temperature-dependent, so gauges have to be designed to compensate against temperature variations. Hence, strain gauges are material-specific in order to provide correct amount of temperature compensation [5]. In addition, electromagnetic interference may induce noise to measurements. While traditional strain gauges provide an effective way for determining strain and stresses, they have some major limitations that restrict their applicability.

The introduction of laser and the development of powerful and affordable computers capable of fast and complex data processing have contributed to the increasing popularity of optical strain measurement methods. Traditional strain gauges are challenged by novel fiber-optic strain gauges and full field optical methods. In fiber-optic strain gauge measurement, an optical fiber is rigidly attached to the measurement object. When the object is deformed, it forces the optical fiber to contract or elongate. The strain measurement principle can be based on various optical phenomena, including interferometry, scattering or diffraction [6]. The deformation of the fiber causes a phase or a wavelength shift of light propagating in the fiber. This shift is used as a measure of strain.

Compared to traditional strain gauges, fiber-optic strain gauges are immune to electromagnetic interference and do not pose a combustion danger. In addition, many measurement signals can be serially multiplexed and transmitted requiring only a single fiber. The strain can be measured cumulatively, at discrete locations, or evenly distributed along the fiber [6]. This makes monitoring strains in large objects, like bridges, oil pipes and ships, convenient. However, while fiber-optic strain gauges are more advanced than traditional strain gauges, they can provide measurements in only one dimension, along the fiber.

The main advantages of other optical methods, including electronic speckle pattern interferometry (ESPI), shearography and digital image correlation (DIC), include their non-contact, non-destructive nature and ability to provide full-field data. In addition, they can be applied to a wide range of materials. The measurement principle can be based on detecting light phase shifts using interferometry, like in ESPI and shearography, or on cross-correlation of image subsets, like in DIC. In general, optical methods have very high sensitivity and good dynamic range [5, 7]. Non-contact measurement reduces preparation time and makes possible to measure even very delicate objects, like artwork with very vulnerable paint layers [8, 9].

Full-field data further speeds up measurements as the whole region of interest can be recorded at once. In addition, full-field data allows easy detection of strain and stress

concentrations. This makes optical methods attractive for quality control applications because material defects, including delaminations in composite structures [5] and fatigue in metals [10], often induce stress and strain concentrations. Furthermore, because measurement data can be represented as a digital image, already existing image-processing methods, like different filters, can be easily applied.

Compared to strain gauges, the investment cost of optical measurement systems is significantly higher. In addition, the required data processing is more complex. However, the processing steps and result evaluation can be automated using general software engineering techniques. The need for human interpretation can be minimized, which helps to reduce the potential user-dependent bias on results [5].

1.2 Strain measurements using electronic speckle pattern interferometry

Electronic speckle pattern interferometry is an optical method for obtaining whole field information about surface displacements [11]. The basic principle of ESPI is to illuminate the surface of a test object with two coherent laser beams and to record the resulting reflected interference pattern using a digital camera [12].

When the test object is deformed, surface displacements occur. Displacements cause phase changes in the recorded interference pattern. When measurements are taken before and after object deformation, these phase changes can be calculated separately for each pixel. The resulting map of phase change, commonly called simply as the phase map, is directly related to surface displacements along the measurement sensitivity direction [13]. Depending on the ESPI setup geometry used, the measured displacements can be either in-plane, out-of-plane or some combination.

Surface strains could be directly measured using shearography, an optical technique closely related to ESPI [14]. However, shearography recording is dominated by surface rotation effects that appear much larger than in-plane strain components. This makes extracting in-plane strain information very challenging and impractical [15, 16]. On the other hand, strain field can also be calculated by numerically differentiating the ESPI displacement field [17]. The differentiation process, however, amplifies any measurement noise present and thus deteriorates the quality of strain field. Hence, displacement data should be carefully filtered prior to strain calculation.

The raw ESPI phase map contains 2π phase jumps due to the nature of phase calculation process and is called wrapped. These discontinuities would cause filtering errors and also distort strain calculation at locations close to phase jumps. The phase map must be unwrapped in order to form continuous phase and displacement fields [18]. However, measurement noise and decorrelation effects make the unwrapping process challenging especially in the presence of large strains, leading to unwrapping errors and consequent

anomalies in displacement field evaluation [15]. These would cause detrimental effects on the subsequent strain calculation. Hence, effective strain evaluation requires overcoming the challenges related to both filtering and unwrapping.

One way to overcome the filtering distortion is to decompose the phase data into its sine and cosine components, both of which are continuous functions. They can be filtered separately and then used to reconstruct the filtered, undistorted phase [19]. While this filtering scheme is effective for noise reduction, it does not guarantee error-free unwrapping. It would thus be tempting to omit the unwrapping step entirely. One way to achieve this is to unwrap the phase map locally so that strain is not calculated across a phase jump [20]. While effective, this method is limited to only modest strain values.

An alternative approach explored in this thesis is to represent the measured phase angles as phasors [21]. In phasor format the phase is expressed as a complex number with unit magnitude and phase angle ϕ as the argument. The real and imaginary parts of the phasor are $\cos(\phi)$ and $\sin(\phi)$, respectively. Thus, the phasor-formatted data appears continuous and can be filtered without distortions. However, filtering must be done carefully, because excessive filtering can lead to data smearing effects and reduction in spatial resolution. The method developed in this thesis is based on a repetitive filtering scheme [19] where a moderate filtering step is applied on the data multiple times. Such an approach leads to very powerful filtering effect, while preserving the spatial details better than a heavier single-step filter. Specific attention is given on achieving good performance in high strain areas.

1.3 Novel measurement setup

The fundamental requirement for high coherence restricts the choice of illumination source for ESPI. Unfortunately, typical high-coherence lasers tend to be very costly and bulky. During the last decades laser diodes have become very popular and affordable. In general laser diodes are economical, compact and have good power efficiency. However, they suffer from broad wavelength spectrum, which directly limits their coherence length. Typical coherence lengths of basic laser diodes range from sub-millimeters to a couple of millimeters. On the contrary, typical ESPI measurement systems require a coherence length in the order of several centimeters. Thus, basic laser diodes as such are not applicable to common ESPI applications. However, laser diodes with additional output spectrum control exist. Such single-frequency laser diodes have limited, narrow emission linewidth and consequently higher coherence length than basic laser diodes [22]. However, single-frequency laser diodes are multiple times more costly than basic laser diodes [23].

In addition to cost advantage, the compactness and low power consumption make laser diodes attractive for potential portable measurement systems. So far, most ESPI measurement systems have been designed for fixed location laboratory use. Portable

ESPI systems would be useful for many applications, as demonstrated examples include inspection of paintings [9], gas pipelines [24] and composite panels [25]. However, in order to apply basic laser diodes to ESPI, the major requirement for long coherence length has to be addressed. Diffraction gratings can provide an effective solution [26, 27]. Some ESPI systems based on a combination of a laser diode and a diffraction grating have already been demonstrated [24, 27]. These realizations have relied on transmission type diffraction gratings. Transmission diffraction gratings are attractive because they enable a simple geometry and flexible tuning. However, they suffer from very low light efficiency. An alternative solution investigated in this thesis is to use a reflection type grating that has a significantly higher efficiency than transmission gratings.

1.4 Thesis scope and structure

The main objectives of the thesis are:

1) To develop a strain calculation algorithm based on phasor formatted ESPI data
2) To demonstrate a novel ESPI setup using a compact, limited coherence illumination source.

The emphasis for the strain calculation algorithm is to achieve good performance especially in the presence of high strains. The purpose for hardware development is to illustrate the ability for achieving high quality results with novel, more affordable components, and to make the method more attractive to portable systems.

Chapter 2 covers the theoretical background of ESPI. Chapter 3 addresses aspects of filtering ESPI phase and strain data and describes the developed strain calculation algorithm. The novel ESPI setup development is covered in Chapter 4. Chapter 5 discusses experimental design and validation. The corresponding experimental results are shown and discussed in Chapter 6, and conclusions are finally made in Chapter 7.

2. THEORETICAL BACKGROUND

The chapter begins with a discussion of the important concepts of interferometry and speckle phenomenon that are necessary for understanding the physics behind ESPI. The ESPI measurement principle is then introduced, followed by a description of phase stepping and phase unwrapping that are key steps for extracting meaningful quantitative data from measurements. ESPI noise characteristics are then addressed, and the details of the phasor data format shown.

2.1 Basics of interferometry

Interferometry is a general term for techniques that utilize interference phenomenon for accurate measurements of various quantities. For example, in interferometric distance measurements light is used as an extremely sensitive and accurate ruler. When two or more similar waves are superposed, they interfere. Waves that are in phase interfere constructively, while the interference of the waves that are out of phase is destructive. In order to interfere, the waves must meet certain criteria. In practice, the superposed waves must originate from a common source and cannot have mutually orthogonal polarization states [7]. Coherence is a fundamental requirement for interference. The characteristics and importance of coherence are discussed in detail in chapter 4.

Optical path length (OPL) is the physical path length of light weighted by the reftactive index of the propagation medium. If the refractive index along the entire path is constant, the optical path length is:

$$OPL = nd, \tag{2.1}$$

where the physical length of the path d is weighted by the refractive index of the propagation medium n. In many interferometric measurements the propagation medium is air with n close to unity, and the OPL can be approximated simply as the physical path length.

In a typical interferometric measurement setup a laser beam is divided into two paths using a beam splitter, and later recombined to make them interfere. One of the paths is designated as the reference path and the other one as the object path. In the measurement the studied phenomenon alters the length of the object path or the lengths of both paths. When a light wave propagates, its phase translates along the propagation direction. A change in optical distance by one wavelength causes a 2π change in phase.

Hence, a relative change in the optical path difference (OPD) between the interferometer arms creates a phase difference ϕ:

$$\phi = 2\pi \frac{\Delta OPD}{\lambda}, \tag{2.2}$$

where λ is the wavelength of the light used.

Consider the interference of two harmonic plane waves that travel in the same direction. If the interfering waves have the same wavelength, it can be shown [28] that the intensity of the resulting wave I_S is:

$$I_S = I_A + I_B + 2\sqrt{I_A I_B}\cos(\phi) = I_{avg}(1 + I_{mod}\cos(\phi)), \tag{2.3}$$

where I_A and I_B are the intensities of the original waves, ϕ is the phase difference between them, $I_{avg} = I_A + I_B$ is the average intensity and $I_{mod} = 2\sqrt{I_A I_B}/(I_A + I_B)$ is the intensity modulation. Equation (2.3) shows that the intensity of the resulting wave is directly related with the phase difference between the original waves. Hence, the measurement of the intensities of the original waves and the resulting wave provides a method for assessing the path length difference between the interferometer arms. This forms the basis for all interferometric measurements; the path length difference between the two light beams is transformed into easily measurable intensity.

A careful investigation of equations (2.2) and (2.3) reveals a significant restriction in interferometric measurements. The phase difference term in equation (2.3) is located in the argument of a cosine function. Because cosine is a periodic function, multiple phase differences can lead to same measured intensity. Correspondingly, optical path differences separated by a multiple of λ will lead to same result. In addition, cosine is an even function, so distinction between negative and positive displacement cannot be made based on the measurement alone. Furthermore, the cosine function is highly nonlinear for argument values close to multiples of π, which makes the detection of peaks from intensities challenging [29]. If the direction of displacement is known, the measurements are unambiguous but only up to the wavelength of the laser used, which is much smaller range than what is required in most applications. In modern ESPI systems these restrictions are overcome using phase stepping and phase unwrapping techniques that will be discussed later.

2.2 Speckle phenomenon

Optical roughness indicates surface variations that are larger than the wavelength of light [30]. An object with an optically rough surface reflects light diffusively without significant specular reflection. This means that every point on the surface scatters incoming light in all directions. Consequently, every point in front of such surface receives light from all points on the surface [11]. The reflected interference pattern has

completely random phase and thus random intensity distribution. The pattern consists of grainy dots of varying intensity called speckles and is known as objective speckle pattern [31]. If the reflected interference pattern is imaged using a lens, then every point on the image surface receives light from only a small area on the object surface, and is known as subjective speckle pattern [11, 32]. The appearance of the subjective speckle pattern is still random, as each speckle is formed due to interference of several waves that have travelled slightly different distances and thus have different phases [32].

The speckle pattern carries important information about the surface. When the object is deformed, the movements of surface cause the path lengths of light to change, which alters the speckle pattern. If the intensity is measured before and after deformation, the corresponding change in the intensity of each subjective speckle can be calculated and related to phase difference. The resulting map of phase differences can be used to determine the corresponding path length changes and thus to form a map of surface displacements, provided that the geometry of the system is known. If the object surface is illuminated with two laser beams, the resulting superimposed speckle patterns interfere and form another speckle pattern. Then the intensity and thus the phase distribution of the formed speckle pattern depend on the relative phases of the original patterns [11]. Figure 2.1 shows an example of a speckle pattern, recorded using a monochrome camera and displayed in green to illustrate the color of the laser. Surface roughness makes the interference pattern appear grainy. The bright pixels in the pattern correspond to constructive interference, while dark pixels result from destructive interference.

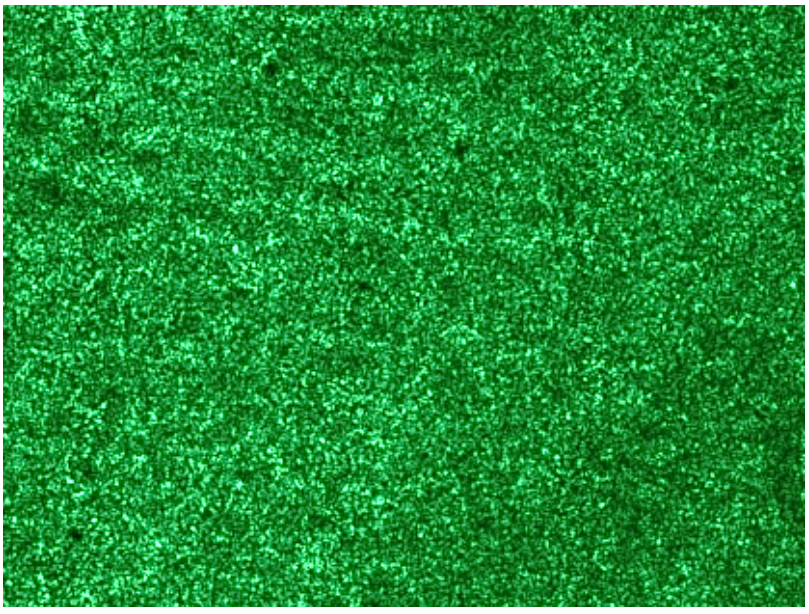

Figure 2.1 *Recorded in-plane ESPI interference speckle pattern.*

The size of subjective speckles depends on the imaging system, and can be defined in many ways. Cloud [33] uses a definition that the size equals the distance between the centers of adjacent bright or dark speckles. In this case the size of subjective speckles (S) on the image plane can be estimated using equation [33]:

$$S = \frac{\lambda f}{d_l}\left(1 + \frac{d_i}{d_o}\right) = \lambda f\#(1 + M), \tag{2.4}$$

where f and d_l are the focal length and the diameter of the imaging lens aperture, respectively, d_o and d_i are the object and image distances, respectively, $f\# = f/d_l$ is the lens f-number and $M = d_i/d_o$ is the image magnification. Hence, the speckle size depends on the laser wavelength and the properties of the imaging system. As the laser wavelength is often fixed, the speckle size is controlled by changing the aperture size and the magnification of the imaging objective.

Speckle size should be tuned to be approximately equal with the camera pixel size. If speckles were much larger than pixels, measurement resolution would suffer. On the other hand, if speckles were much smaller than pixels, averaging effects would deteriorate measurements by reducing fringe modulation [33]. When speckle size is optimized, each pixel ideally acts as an independent interferometer. This is what allows full field deformation data to be extracted in ESPI.

2.3 Measurement principle

Figure 2.2 shows a typical ESPI setup with in-plane sensitivity. A highly coherent laser beam is diverged using a lens integrated in the laser housing and then collimated by a second lens. The collimated laser beam is evenly divided into two paths using a non-polarizing 50/50 beam splitter. The transmitted and reflected laser beams are further reflected from a fixed and piezo mirror, respectively. Finally, the beams overlap and illuminate the surface of a test object. A digital camera is used to image the intensity of the speckle pattern that is diffusively reflected from the object surface.

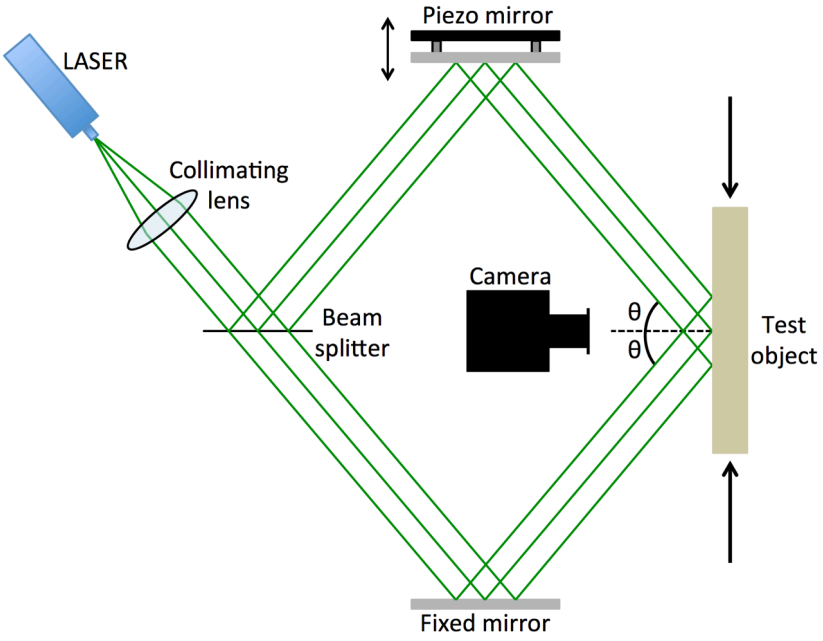

Figure 2.2 *In-plane ESPI measurement setup.*

Figure 2.3 illustrates the illumination and observation (wave) vectors for in-plane ESPI. The two collimated laser beams illuminate the object surface, and the illumination and the observation directions lie in the xz-plane. Lets consider the center point in the illuminated area. The illumination vectors of the beams $\boldsymbol{k}_1$ and $\boldsymbol{k}_2$ are:

$$\boldsymbol{k}_1 = \frac{2\pi}{\lambda}(\sin(\theta_1), 0, -\cos(\theta_1)), \tag{2.5}$$

$$\boldsymbol{k}_2 = \frac{2\pi}{\lambda}(-\sin(\theta_2), 0, -\cos(\theta_2)), \tag{2.6}$$

where θ_1 and θ_2 are the illumination angles for beams 1 and 2 respectively. The waves reflected diffusively from the center point through the imaging system are characterized by the observation vector $\boldsymbol{k}_o$, which is defined by the location of camera and the orientation of the field of view (FOV) of its sensor array. When the object is loaded, its surface is deformed. The surface deformation at the center point is characterized by a deformation vector $\boldsymbol{d}$:

$$\boldsymbol{d} = (d_x, d_y, d_z)', \tag{2.7}$$

where d_x, d_y and d_z are the deformation components in each axis.

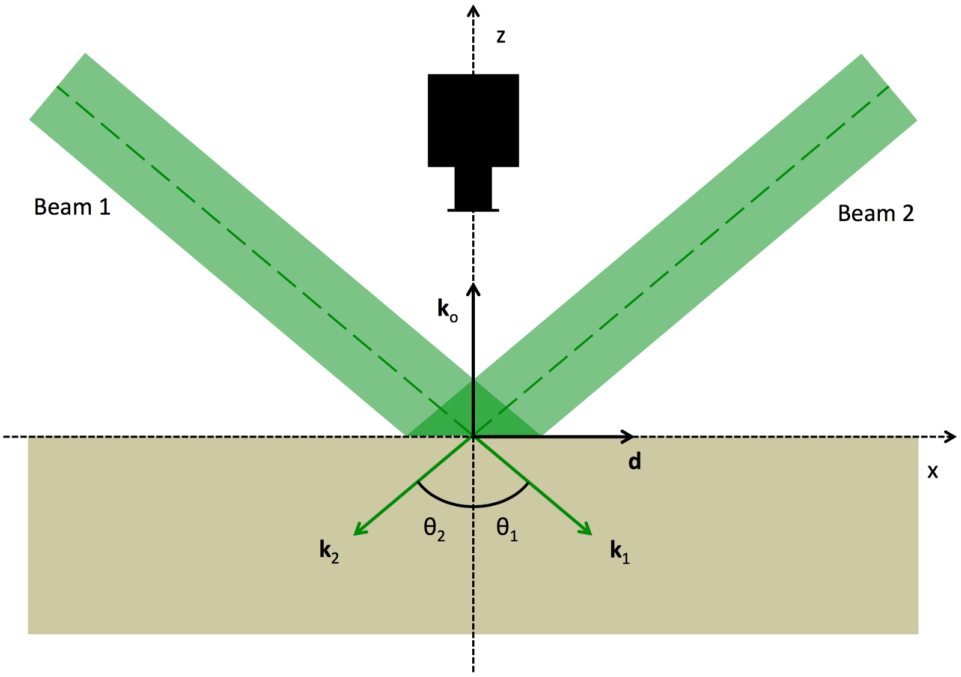

Figure 2.3 *Sensitivity characterization of in-plane ESPI.*

The deformation causes phase differences in both beams [30]:

$$\phi_1 = \boldsymbol{k}_1\boldsymbol{d} - \boldsymbol{k}_o\boldsymbol{d}, \tag{2.8}$$

$$\phi_2 = \boldsymbol{k}_2\boldsymbol{d} - \boldsymbol{k}_o\boldsymbol{d}, \tag{2.9}$$

where ϕ_1 and ϕ_2 are the phase differences in beams 1 and 2, respectively.

The observed relative phase difference $\Delta\phi$ between the beams is thus:

$$\Delta\phi = \phi_1 - \phi_2 = \boldsymbol{k}_1\boldsymbol{d} - \boldsymbol{k}_2\boldsymbol{d} = (\boldsymbol{k}_1 - \boldsymbol{k}_2)\boldsymbol{d} = \boldsymbol{K}_s\boldsymbol{d}, \tag{2.10}$$

$$\Delta\phi = \frac{2\pi}{\lambda}[(\sin(\theta_1) + \sin(\theta_2)d_x + (\cos(\theta_2) - \cos(\theta_1))d_z], \tag{2.11}$$

where $\boldsymbol{K}_s = \boldsymbol{k}_1 - \boldsymbol{k}_2$ is the measurement sensitivity vector.

Equation (2.10) shows that the relative phase difference is independent of the observation direction. For symmetric illumination condition $\theta = \theta_1 = \theta_2$ equation (2.11) reduces to:

$$\Delta\phi = \frac{4\pi d_x}{\lambda}\sin(\theta). \tag{2.12}$$

Using symmetric illumination in xz-plane the phase change indicates purely in-plane displacements in x-axis – i.e. the interferometer's sensitivity vector is in x-direction. Measurement sensitivity and thus resolution can be increased by increasing the

illumination angles. On the other hand, an increase in angles reduces light intensity, as the illuminated area becomes more elliptical. As a compromise, the illumination angles are commonly kept around 45°.

The illumination and observation directions vary within the illuminated area depending on the location on the surface. Typically, however, the distances between the laser, the object and the camera are much larger than the dimensions of the region of interest on the object surface. Then the interference between the reflected waves originating from the different beams and propagating towards the camera is very close to collinear [32]. In such a case the sensitivity can be approximated uniform across the illuminated area [30]. The relative phase change can be calculated for each pixel from the intensities of the speckle patterns recorded before and after deformation, using the phase stepping method that will be discussed in the next section.

2.4 Phase stepping

The intensities in speckle patterns behave according to equation (2.3) and thus have three unknowns, namely the average and the modulation intensities and the phase difference. The basic idea of temporal phase stepping is to modify the phase difference by a known amount, and record a set of independent intensity measurements. The phase difference is introduced by changing the path length of one of the beams by altering the voltage of the piezoelectric transducer (PZT) attached to one of the mirrors in the ESPI setup. The movement of the PZT can be calibrated to cause a desired phase shift. There are three unknowns, so at least three measurements are needed. The most common phase stepping technique uses four steps, each at 90° phase increment [21]. A set of four images is taken before and after deformation. Each set will then have form:

$$I_1 = I_{avg} + I_{mod}\cos(\phi), \tag{2.13}$$

$$I_2 = I_{avg} + I_{mod}\cos\left(\phi + \frac{\pi}{2}\right), \tag{2.14}$$

$$I_3 = I_{avg} + I_{mod}\cos(\phi + \pi), \tag{2.15}$$

$$I_4 = I_{avg} + I_{mod}\cos\left(\phi + \frac{3\pi}{2}\right), \tag{2.16}$$

where I_1, I_2, I_3 and I_4 are the phase stepped intensities measured separately for each pixel. Using basic trigonometric relations for sine and cosine, the phase angle can be calculated as [21]:

$$\phi = \arctan\left(\frac{\sin(\phi)}{\cos(\phi)}\right) = \arctan\left(\frac{I_4 - I_2}{I_1 - I_3}\right). \tag{2.17}$$

By calculating the phase angle before and after deformation for each pixel, the relative phase difference $\Delta\phi$ can be determined by simply subtracting the phase angles. The four-step phase-stepping method is simple and robust.

Because tangent is a periodic function, the calculated phase differences have modulo-π form. With the two-argument atan2-function the phase range can be extended to modulo-2π. Still, for any displacement that leads to a phase difference larger than ±π, the determined relative phase difference value differs from the correct one by an integral multiple of 2π. The phenomenon is known as phase wrapping and causes the calculated map of relative phase difference to have sharp discontinuities at locations where the relative phase difference exceeds value ±π by an integral multiple of 2π. Figure 2.4 illustrates the differences between direct intensity subtraction and phase stepping method. The data shown is synthetic and based on the Matlab "Peaks" function. Phase stepping overcomes the directional ambiguity problem discussed previously. Phase discontinuities can be seen as sharp black-white interfaces. The altering dark and bright areas are called fringes. In order to obtain continuous phase and displacement maps and to further calculate surface strains, the discontinuities have to be corrected by a phase unwrapping process.

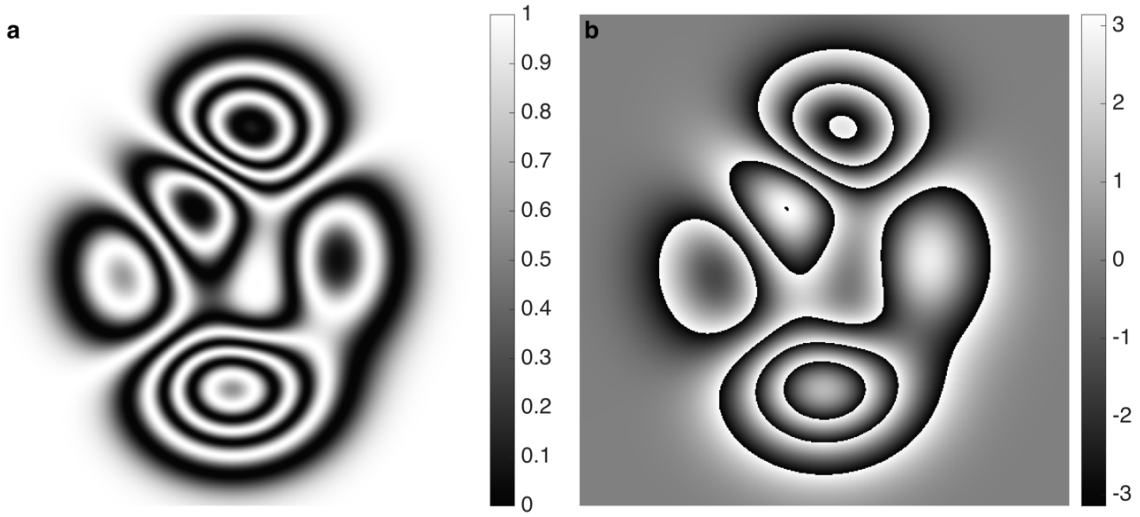

Figure 2.4 *Illustration of phase distribution using (a) absolute value of intensity subtraction, units in fractions of maximum intensity, (b) phase stepping method, units in radians.*

2.5 Phase unwrapping

The phase wrapping phenomenon is common in various fields of engineering. In addition to ESPI and other optical interferometry, wrapping issues are present for example in satellite radar terrain topography measurements [34], and magnetic resonance imaging (MRI) [35]. The general requirement for phase continuity is that the phase difference between adjacent pixels has to be less than π [18]. The basic idea of unwrapping is to scan the image containing wrapped phase distribution, detect the phase

differences over the threshold, and correct them by adding or subtracting the required multiple of 2π. Figure 2.5 shows the unwrapped phase map for the same synthetic data shown in Figure 2.4.

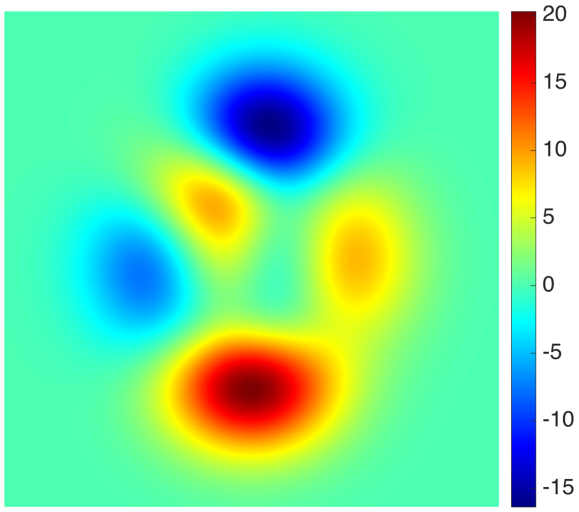

Figure 2.5 *Illustration of unwrapped phase map, units in radians.*

Due to the prevalence of phase wrapping phenomenon, much effort has been put on developing phase unwrapping algorithms [18]. Most unwrapping algorithms follow a pre-defined path [36]. The simplest algorithms scan the image line by line – every time a phase jump is detected, all the remaining pixels in the corresponding line are shifted by the required amount. If the data are clean, the unwrapping process is trivial. However, all experimental data contain noise. Unwrapping methods that have been developed for clean data are very sensitive to noise [37]. Noise distorts phase values, which leads to phase unwrapping errors. Some true phase jumps may not be detected, and some distorted areas may be wrongly interpreted to have discontinuities and thus shifted incorrectly. In simple algorithms unwrapping errors can propagate and cover large areas on the phase map. In more advanced algorithms, like the widely used Goldstein's branch cut algorithm [34], problem areas are detected, isolated, and neglected or unwrapped last to avoid error propagation [36]. Still, high levels of noise significantly deteriorate the quality of unwrapped phase map.

2.6 Noise characteristics

The differential path geometry makes ESPI very prone to various environmental disturbances. Any relative difference in the optical path length of the interferometer arms directly affects the measured signal. Vibrations, convective air currents, humidity, pressure and temperature gradients are common sources of noise in ESPI measurements [5]. In addition, ambient and stray light can cause unwanted noise signals. Hence,

measurements should be done in laboratory conditions. A dark, closed space with vibration isolation can greatly improve the measurement quality.

When the test object is deformed, the movements of the object surface cause the reflected speckles to translate relative to the pixels in the camera sensor. Consequently, the correlation between the intensity patterns recorded before and after deformation is reduced. This phenomenon is known as speckle decorrelation and is the most important factor affecting the measurement quality in ESPI [38], aside of the measurement conditions. The speckle decorrelation resulting due to large displacements introduces additional noise that deteriorates the signal-to-noise ratio (SNR) of the ESPI data [15]. This is a significant problem because accurate detection of high strain concentrations is of high importance for quality control applications.

The rectangular shape of camera pixels is not ideal for capturing complex shaped speckles, which further reduces the measurement SNR. In addition, the movements of the PZT may vary and the phase steps can drift away from the ideal 90° angle. As a result, ESPI noise levels are inherently high, making the unwrapping process very challenging. Thus, it is crucial to filter phase data before unwrapping. However, high noise levels can restrict the applicability of filters – a modest filtering may not be enough for successful unwrapping, while too strong filtering may distort the fine details in phase data and lead to smearing effects [37].

2.7 Phasor formatted data for strain calculations

Unlike in topography measurements and MRI, for ESPI strain measurements the unwrapped phase map is not the primary goal, but rather only a necessary intermediate result. Existing approaches require a continuous displacement field in order to determine the strain field without distortions. If wrapped data were used, numerical differentiation performed over discontinuities would lead to corrupted strain values at the locations of phase jumps. Bypassing the unwrapping step can simplify and speed up the strain calculation process and avoid potential unwrapping errors. The use of phasor format data [21] provides a simple and convenient solution for this. A phase angle ϕ can be related to a complex number Φ:

$$\Phi = \cos(\phi) + i\sin(\phi) = e^{i\phi}, \tag{2.18}$$

where $i = \sqrt{-1}$. The phase angle ϕ is thus the argument of the complex number Φ:

$$\phi = \arg(\Phi) = \arg\left(e^{i\phi}\right). \tag{2.19}$$

Phase subtraction in real domain is analogous to phase multiplication by a complex conjugate in complex domain:

$$\phi_A - \phi_B = \arg\left(e^{i(\phi_A - \phi_B)}\right) = \arg\left(e^{i\phi_A} e^{-i\phi_B}\right) = \arg(\Phi_A \Phi_B^*), \tag{2.20}$$

where $\Phi^* = e^{-i\phi}$ is the complex conjugate of Φ. Using real-valued wrapped data, the subtraction of phase values of points located across the phase jumps may lead to wrong results that are not contained within $\pm\pi$. On the other hand, subtraction using complex domain automatically keeps the result within the range $[-\pi, \pi)$. For example, consider a case where pixels p_A and p_B lie across a phase jump. Let the corresponding phase values be $\phi_A = -0.9\pi$ and $\phi_B = 0.85\pi$. Using real-valued wrapped data, the phase difference $\phi_A - \phi_B = -1.75\pi \notin [-\pi, \pi)$. However, if phasor format is used, the same calculation yields the result $\phi_A - \phi_B = 0.25\pi \in [-\pi, \pi)$.

In ESPI, the numerical calculation of the strain between any points *A* and *B* involves subtracting the in-plane displacements at these points and dividing the result by the physical separation of the points. Thus, the strain ε_{AB} is directly proportional to the difference of the relative phase change between the points:

$$\varepsilon_{AB} \sim (\Delta\phi_A - \Delta\phi_B) \sim \Delta\Phi_A \Delta\Phi_B^*. \tag{2.21}$$

The exact strain value can be determined when the ESPI geometry and the distance between the points *A* and *B* is known.

Measurement noise has a significant effect on the quality of ESPI strain map because the numerical differentiation amplifies any phase uncertainties. Thus, noisy phase data has to be filtered before strain calculation step. When the phase map is transformed into complex domain, both the real and the imaginary parts of the phase map are continuous, so the phase map appears continuous. The continuous nature of the phasor format makes the application of common filters convenient – filtering errors due to phase jump distortion are avoided. When the goal is at measuring high strain concentrations, the filtering is of utmost importance due to increased speckle decorrelation noise.

3. STRAIN CALCULATION ALGORITHM

The chapter begins by introducing the basic characteristics of filtering image type data. ESPI phase map filtering is then considered. Both traditionally used and some newer, more advanced filters are discussed. The advantages and drawbacks of each filter are presented, and more appropriate filtering for data containing high phase gradients is introduced. Next, strain map calculation and filtering is studied. The drawbacks of existing methods are emphasized, and a better alternative presented. Finally, the steps and details of the proposed strain calculation algorithm are introduced.

3.1 Image data filtering

The goal of image filtering is to improve the image data for a specific purpose. Filtering can be done optically by adding a physical filter element as a part of the imaging system, or digitally by manipulating the pixel values of a digital image. With modern computers, digital filtering is fast, powerful and flexible with almost endless possibilities. Common digital filters include e.g. noise removal, color filtering, sharpening, blurring, shading and edge detection.

Filters may be applied in spatial or frequency domain, and filtering may be performed pixelwise, locally or globally [39]. Pixelwise filtering could be for example the extraction of red color component from an RGB-format image, or adjusting image brightness. In global filtering each pixel in the filtered image is affected by the data content of the entire original image. Many global filters are based on Fourier transform, where the original image is transformed from spatial domain to frequency domain that represents the image spectrum. Image manipulation is then performed in the frequency domain where calculations are often simpler. Finally, the manipulated, filtered image is transformed back to spatial domain.

Many filters, however, are local. In local filtering the value of each image pixel is manipulated depending on the values within a local neighbourhood. Filtering may be linear or nonlinear. In linear filtering the filtered output is a linear combination of the neighbourhood pixels. Filtering function is expressed by a filtering matrix, kernel. Mathematically expressed, linear filtering is a convolution between the image matrix and filtering kernel. As an example, consider an image G that is a 4x4 matrix:

$$G = \begin{bmatrix} a & b & c & d \\ e & f & g & h \\ i & j & k & l \\ m & n & o & p \end{bmatrix}. \quad (3.1)$$

Let the filtering kernel *F* be a 3x3 matrix:

$$F = \begin{bmatrix} 1 & 2 & 3 \\ 4 & 5 & 6 \\ 7 & 8 & 9 \end{bmatrix}. \quad (3.2)$$

In the original image the pixel $G_{3,3} = k$. In the filtering process the convolution filtering kernel is first centered to *k* and the values in its neighbourhood are weighted pixelwise by the corresponding kernel values. The new, filtered value of *k* is obtained by summing the weighted neighbourhood values:

$$G_{3,3}^{f} = 1f + 2g + 3h + 4j + 5k + 6l + 7n + 8o + 9p. \quad (3.3)$$

The process is performed for each pixel in the image. Convolution filtering often involves using pixels that extend over the edges of the image matrix. In such cases the edges of the image can be ignored, which makes the filtered image to have smaller dimensions than the original one. It is also possible to calculate the convolution by using only the available pixels, or for example mirror-reflect the image across the image borders.

Mean filter is a simple linear filter for removing noise in an image. It involves replacing the value of each pixel by the average of the pixels within the corresponding kernel. The filtering kernel is a matrix with even weights. For example a 3x3 mean filtering kernel F_{3x3}^{mean} is:

$$F_{3x3}^{mean} = \frac{1}{9}\begin{bmatrix} 1 & 1 & 1 \\ 1 & 1 & 1 \\ 1 & 1 & 1 \end{bmatrix}. \quad (3.4)$$

The filtering kernel has to be normalized, i.e. the sum of the elements has to be one, in order to keep the image brightness unchanged. In addition to noise removal, mean filter smoothens and blurs the image, suppressing intensity variations between adjacent pixels. Thus, mean filter can be categorized as a low-pass filter. The larger the kernel, the more effective the noise removal and blurring are. Gaussian filter is another common low-pass filter. It can be described as a weighted average filter where the weights have a Gaussian distribution; pixels nearest to the kernel center are weighted most and remote pixels least. Median filter, on the other hand, is a common nonlinear filter where the median of the filtering kernel is used to replace the value of the center pixel.

3.2 Phase map filtering methods

Mean and median filters have been routinely used for filtering wrapped ESPI phase maps [5, 21, 30, 39]. Before the introduction of sine-cosine transformation, mean filter and other low-pass filters were troublesome to apply because they would distort the phase discontinuities. The reason for this is that both noise and true phase jumps are characterized by high spatial frequencies [40]. Median filter was advantageous, as it did not distort the phase discontinuities as severely as low-pass filters [5, 39]. However, when combined with sine-cosine transformation, mean filtering does not have this problem anymore. In speckle interferometry the SNR is naturally very low due to speckle noise. For such low quality signals mean filter performs better than median filter [5]. In addition, mean filtering is faster to process as a linear operation.

The main drawback of basic mean filtering is that it is not adaptive. In addition, mean filtering can severely affect the data. This is because removing high level of noise requires a large kernel, which tends to significantly blur the image and reduce spatial resolution. This is detrimental, because high spatial resolution is crucial for detecting localized strain concentrations and thus potential mechanical defects. Because strain concentrations are linked with significant speckle decorrelation noise, the basic mean filtering is not an ideal tool for noise removal in ESPI.

During the last two decades, many advanced filtering methods have been developed for wrapped phase data. Ströbel [21] introduced an ESPI phase map filtering method based on weighted phasor mean filtering. He expressed the phase map in phasor format and weighted the phasor values by corresponding phase angle modulation amplitude values. The idea is that pixels with high modulation are likely more accurate and should thus have a greater influence than pixels with low modulation. While the weighting is self-adaptive, the size of the filtering kernel is fixed. In addition, in the presence of high spatial gradients the required kernel size may be too large to maintain sufficiently high spatial resolution.

An and Schajer [41] developed a selective phase filtering method with more comprehensive pixel quality estimation. They evaluated the quality of pixels using three measures: saturation, variance and visibility. If a certain pixel has a maximum gray level value in any of the captured images, it is considered saturated. Variance parameter measures how much the phase of a pixel deviates from the values in a local neighbourhood. Visibility refers to phase angle modulation intensity and is closely related with the modulation amplitude parameter used by Ströbel. If a pixel is saturated, has a high variance or a low visibility, it is considered defective. The defective pixels are replaced by the values of surrounding good pixels using multidimensional interpolation. The advantage of this method is that the noise in defective pixels is not spread around. However, the interpolation process leaves some high-frequency noise. As the authors report [41], an improved result is obtained if a modest mean filtering is

applied after the interpolation step. The presence of high phase gradients has no effect on intensity saturation and visibility values, but variance is directly affected for two reasons. First, high phase gradients directly cause larger differences between the neighbouring pixel values. In addition, the increased speckle decorrelation noise further increases these variations. If a fixed threshold value is used for variance evaluation, the number of defective pixels directly depends on the size of phase gradients. High phase gradients increase the number of pixels marked as defective, and at the same time less pixels are actually used for extracting the information for excluded pixels. It is clear that the spatial resolution suffers and the applicability of the method is limited in the presence of very high strain concentrations.

Bioucas et al. [37] introduced an adaptive nonlinear phase filtering scheme based on local polynomial approximation (LPA). The size of the filtering window is adjusted based on the smoothness of the data; large areas are used where the phase varies smoothly, while the window size is more restricted in the presence of abrupt changes like phase jumps. The smoothness of the data is estimated using a zero-order LPA, while the actual filtered phase is calculated using a first-order LPA. The method is effective and detail preserving but also relatively complex, which increases the computation times.

Huang et al. [36] aimed at obtaining a noise free unwrapped phase map using a total-variation (TV) based filtering. The method involves first calculating the phase gradients, i.e. strain fields, in x and y directions directly from the wrapped, noisy phase map. This leads to very noisy and distorted strain fields because noise is amplified in the differentiation process and strain calculation errors occur at phase discontinuities. The distorted strain fields are then filtered and corrected using a TV-filtering algorithm. The filtered strain fields are further integrated to get an estimate of the unwrapped phase map. The quality of the unwrapped phase map is then evaluated by comparing it with the original phase map. If needed, the unwrapped phase map is rewrapped and the process repeated iteratively until a satisfying result is obtained. For high-quality signals only a few iterations are required. However, when the SNR of the phase map is reduced, like in the presence of high strain concentrations, the required number of iterations and computation time increase dramatically. In addition, the suitability of the method is limited to phase maps without abrupt changes.

3.3 Optimal phase map filtering of high phase gradient data

As discussed above, the limitation of simple phase filtering methods is their inability to adapt and to handle large phase gradients. More advanced methods, however, may be able to handle data even in the presence of high strain concentrations, but often at the cost of an impractically long processing time. The ability to get results fast and to monitor measurement in real time would be advantageous not only while tuning and optimizing the measurement equipment, but also for many practical applications.

Hence, it would be beneficial to find a filtering method that has the necessary performance for handling high phase gradients but is not overly complex computationally. The repetitive filtering method introduced by Aebischer and Waldner [19] seems attractive for reaching these goals.

In the Aebischer and Waldner's repetitive filtering scheme a simple mean filter with a small kernel is repeatedly applied on the wrapped ESPI phase map. The small kernel ensures that sufficient spatial resolution is preserved. When the simple mean filter is applied multiple times, the least noisy areas become smooth after only one or a few repetitions. For more noisy areas, the required number of repetitions is higher. Luckily, the method is essentially self-adaptive. When the number of filtering repetitions is set high, for example 10, the whole phase map is filtered 10 times. In the areas with little noise, the last iterations have a negligible effect on the phase values, while at the areas of highest noise concentrations the filtering is effective for a larger number of repetitions. As with any filter, filtering errors are possible. Hence, it is important to avoid excessive filtering, which is commonly known to cause fringe smearing. In repetitive filtering scheme some blurring occurs but the effect is much less severe than for a large single step mean filtering. In any case, the number of iterations should be controlled.

It is curious why such a simple filtering method can be so effective that it can challenge many much more sophisticated methods [19]. The reason for this lies in the nature of the noise. Speckle noise is multiplicative, i.e. the measured signal is the true signal multiplied by the noise [42]. Gaussian or additive noise, on the other hand, is summed on top of the true signal. The multiplicative nature of speckle noise restricts the efficiency of simple mean filter and other low-pass filters. However, if a phase map with multiplicative speckle noise is mean filtered, the remaining noise will become additive. In the case of repetitive mean filtering, each repetition makes the remaining noise more and more additive, and thus the filtering becomes more effective [43].

3.4 Strain map calculation and filtering methods

The conventional methods for calculating strain map from ESPI data require an unwrapped displacement map. The displacement map can be calculated from the phase map using equation (2.12) in the following form:

$$d_x = \frac{(\Delta\phi)\lambda}{4\pi \sin(\theta)}. \tag{3.5}$$

The simplest way to calculate strain map is to use direct numerical differentiation. The principal strain component ε_{xx} between between pixels p_i and p_j is the difference in the corresponding x-displacements $d_{x,i}$ and $d_{x,j}$, divided by the separation of the pixels (L_{ij}):

$$\varepsilon_{xx} = \frac{d_{x,i} - d_{x,j}}{L_{ij}}. \tag{3.6}$$

The separation, called gauge length, can be altered depending on the measurement. A short gauge is better for peak strains, while a long gauge provides a more averaged strain value and thus also reduces the level of noise.

The filtered, unwrapped phase map may contain some residual noise that would be amplified in the differentiation process and thus deteriorate the strain field quality. This is why more advanced strain calculation methods, especially least squares surface fitting of the displacement map, have been developed [20, 38]. In linear least squares surface fitting a plane is fitted to the pixel values in a rectangular neighbourhood of each pixel. The strain in the central pixel is then determined from the slope of the fitted plane [20]. The least squares strain calculation is a linear operation, so it can be performed using a convolution in a similar manner as described previously. For example, a 7x7 size least squares convolution kernel F_{7x7}^{LSQ} for the principal strain component ε_{xx} is [20]:

$$F_{7x7}^{LSQ} = \frac{1}{196}\begin{bmatrix} -3 & -2 & -1 & 0 & 1 & 2 & 3 \\ -3 & -2 & -1 & 0 & 1 & 2 & 3 \\ -3 & -2 & -1 & 0 & 1 & 2 & 3 \\ -3 & -2 & -1 & 0 & 1 & 2 & 3 \\ -3 & -2 & -1 & 0 & 1 & 2 & 3 \\ -3 & -2 & -1 & 0 & 1 & 2 & 3 \\ -3 & -2 & -1 & 0 & 1 & 2 & 3 \end{bmatrix}, \tag{3.7}$$

where the fraction 1/196 is a least squares normalization factor. Let's study the least squares convolution operation more carefully. For a central pixel p_i in the studied neighbourhood, the convolution in the center row leads to summation $1 * (p_{i+1} - p_{i-1}) + 2 * (p_{i+2} - p_{i-2}) + 3 * (p_{i+3} - p_{i-3})$. This is essentially a weighted sum of direct strains for the central pixel with different gauge lengths. The weight is linearly increased as a function of gauge length. The least square strain is then a column average of these weighted direct strains. Hence, least squares calculation provides smoothing in addition to strain determination.

In a traditional form, least squares strain calculation requires a continuous displacement map. Cloud improved the technique by introducing local unwrapping [20], where the phase map is pixelwise unwrapped only in a local neighbourhood large enough for the least squares convolution kernel. Because the phase map is not globally unwrapped, the potential unwrapping errors cannot propagate.

The speckle decorrelation related noise is very significant under heavy loads and high strain concentrations. In addition, phase filtering has to be limited in order to avoid fringe distortion. Hence, the filtered phase map contains some residual noise that has to be filtered out in the strain calculation process or from the calculated strain map. This leads to problems especially with the least squares fitting. High level of residual noise

requires a large filtering kernel. However, the maximum kernel size is limited, as the maximum true phase gradient across the filtering window is limited to 2π in local unwrapping. In the presence of measurement noise and because the longest gauge lengths are weighted most, the problem is even more severe. The situation is paradoxical; high strain concentrations cause high levels of noise but at the same time they limit the maximum applicable filtering.

3.5 Optimal strain map filtering for high strain concentrations

The effectiveness of the repetitive phase map mean filtering raises a question whether a similar approach could be used also for strain maps. Using the phasor format, the strain field can be calculated directly from the wrapped phase map, and thus avoid any unwrapping errors. Gauge length must be limited because the phase gradient within the gauge cannot exceed ±π; otherwise the resulting strain value would be falsely wrapped. Central difference strain calculation can be used to achieve a second order accuracy and logical pixel indexing. The central difference strain calculation has a form:

$$\varepsilon_{xx,i} = \frac{\Delta\phi_{i+K} - \Delta\phi_{i-K}}{2K}, \tag{3.8}$$

where $\varepsilon_{xx,i}$ is the strain ε_{xx} in pixel i in units rad/pixel and $2K$ is the gauge length in pixels. In phasor format, the calculation becomes:

$$\mathrm{E}_{xx,i} = (\Delta\Phi_{i+K}\Delta\Phi_{i-1}^{*})^{1/(2K)}, \tag{3.9}$$

where $\mathrm{E}_{xx,i}$ is the phasor format strain corresponding to $\varepsilon_{xx,i}$:

$$\mathrm{E}_{xx,i} = e^{i\varepsilon_{xx,i}}. \tag{3.10}$$

The gauge length can be optimized for given data. In the presence of large phase gradients the gauge length must be limited so that the calculated strains are contained within ±π range limit of the phasor format.

The resulting phasor strain field could then be filtered using the simple repetitive mean filtering scheme. Because strain field does not contain phase jumps and is also more slowly varying than wrapped phase field, it might be possible to use larger filtering kernels. The larger kernels would have a greater filtering effect and thus be useful because the differentiation process amplifies any noise present. The kernel size is not limited in the same way as it is for the least squares filtering, because the kernel and gauge sizes could be controlled independently. However, kernel size obviously has an effect on the spatial resolution.

3.6 Proposed strain calculation algorithm

The strain calculation algorithm proposed and investigated in this thesis is based on the repetitive phasor format mean filtering. The repetitive filtering scheme is applied to both wrapped phase map and calculated raw strain field. The filtering parameters are optimized depending on the data. The steps of the proposed algorithm are listed below.

1) The raw phase map is calculated from the phase stepped intensities recorded before and after deformation
2) The phase map is represented in phasor format
3) A repetitive mean filtering is applied on the raw phasor format phase map. The kernel size is limited to 3x3 in order to preserve good spatial resolution and to maximize the measurable phase gradients. The number of repetitions is adjusted depending on the level of measurement noise. The phasors are renormalized after each repetition.
4) The strain map is calculated pixel by pixel. The gauge length is adjusted depending on the magnitude of phase gradients present.
5) A repetitive mean filtering is applied on the raw phasor format strain field. The kernel size and number of iterations are adjusted depending on the data. The phasors are renormalized after each repetition.
6) The strain values are obtained as the arguments of the phasor formatted strains.

The main goal for the algorithm is to be able to detect high strain concentrations, while maintaining good spatial resolution. It is crucial to renormalize the phase map after each filtering repetition, as the filtering can cause the phasors to be drifted away from the initial unit length. In addition, the low-quality unmodulated pixels are set to have a zero phasor length, so they have no contribution in the filtering process.

The general approach for strain field determination involves first unwrapping the filtered phase map and then calculating the strain field in some way. To the best of knowledge, this is the first time the strain field is calculated directly from wrapped ESPI phase map using phasor format. The only other indication of direct strain determination known to the author is the one proposed by Huang et al. [36]. However, their solution is based on a complex iterative process that requires removing the phase jump and noise distortions from the calculated strain field, then integrating the filtered output to obtain an unwrapped phase map, and repeating the cycle.

4. RELAXING COHERENCE REQUIREMENTS

The chapter begins by describing the general characteristics and importance of coherence, followed by quantitatively investigating the coherence requirements for in-plane ESPI. The operation principles of diffraction gratings are then discussed, and the application of diffraction gratings for relaxing the ESPI coherence requirements is illustrated.

4.1 Characteristics and importance of coherence

Coherence represents the degree of phase correlation in a wave, and can be divided into spatial and temporal types. In a spatially coherent wave the phase difference between any two points in a wavefront remains fixed. Temporally coherent wave, on the other hand, has a fixed phase difference between any two points in the wave along the propagation direction [44]. This means that if two rays within a light beam are originally in phase, they will remain in phase as light propagates. It is important to note that spatial and temporal coherence are independent of each other [45].

Light in traditional illumination sources is created by spontaneous emission, i.e., by random events, and thus is uncorrelated. Laser light, on the other hand, is based on controlled, stimulated emission and is consequently highly correlated [44]. However, no laser is perfectly coherent. The spatial coherence of lasers is improved when the number of transverse modes is restricted. Ideally only the fundamental TEM_{00} mode is oscillating. Such single transverse mode operation is relatively easy to achieve in modern practice [45].

Laser output is often not strictly monochromatic, but rather a distribution of slightly different wavelengths. This occurs when the laser gain bandwidth exceeds the separation of wavelengths that are supported by the laser cavity, i.e., can form a standing wave inside the laser resonator. In such a case laser can have many lasing wavelengths that are separated by a fixed interval [45]. Because of these different wavelengths, the phase evolution in a light beam is not uniform. Hence, the light rays originally in phase will eventually run out of phase. Thus the temporal coherence is restricted by bandwidth.

Figure 4.1 illustrates the interaction of laser beams with different coherence lengths. The top beam in Figure 4.1 has a wide bandwidth and consequently the phases of different wavelengths quickly diverge. The center and bottom beams have smaller bandwidths and thus it takes a longer distance for the beams to dephase.

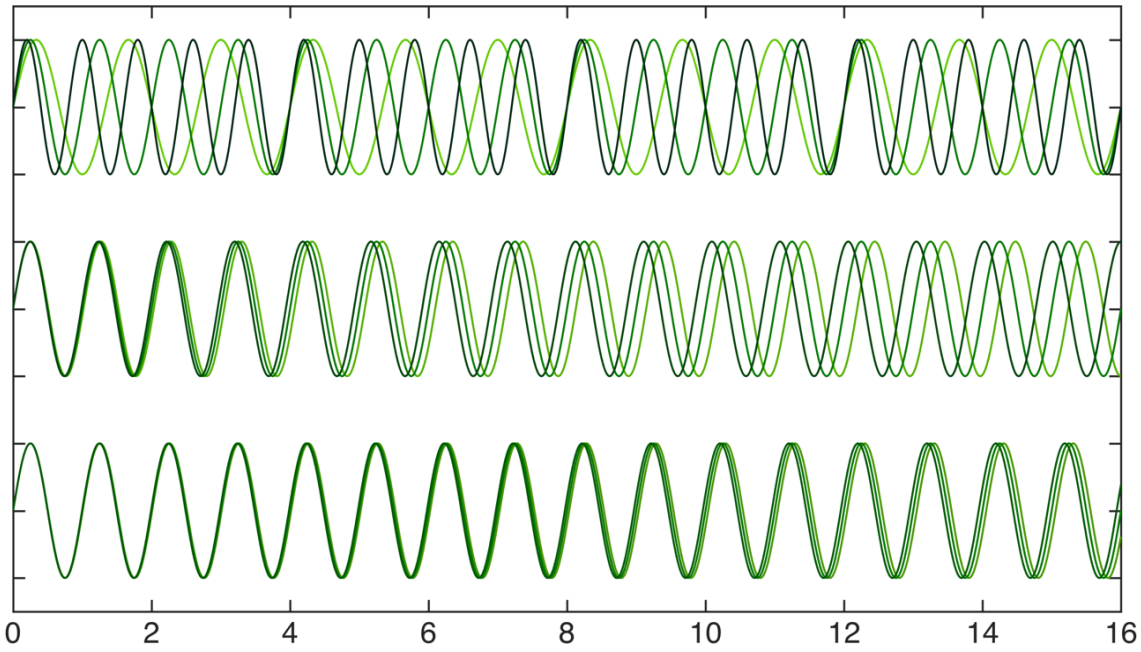

Figure 4.1 *Illustration of laser beams with different coherence lengths. The top beam has the lowest temporal coherence, while the bottom beam has the highest temporal coherence.*

Temporal coherence can be characterized by coherence time and coherence length, measures that are inversely proportional to the laser bandwidth. Coherence time is an interval over which the phase of the light wave can be sensibly defined at a given point in space [46]. The corresponding coherence length is simply the distance the wave propagates during the coherence time. In mathematical form the coherence length (l_c) of light with Gaussian distribution is [47]:

$$l_c = \sqrt{\frac{2\ln 2}{\pi}}\frac{\lambda_0^2}{\Delta\lambda}, \tag{4.1}$$

where λ_0 is the central wavelength and $\Delta\lambda$ is the wavelength bandwidth.

In the context of ESPI the finite coherence length means that when the path length difference between the interfering beams increases, the modulation intensity is reduced. Consequently, the contrast between phase-stepped intensities is reduced and uncertainty in phase angle calculation is increased. Hence, the measurement quality of the measured ESPI phase map varies as a function of path length difference.

Figure 4.1 shows also another interesting phenomenon. When the propagating wavelengths have got out of phase and propagate even further, they eventually return into phase again and the beam becomes coherent again. Such cyclic behaviour occurs when the wavelengths of the component waves in Figure 4.1 have a uniform interval between them. This behaviour would not occur if the wavelengths of the component

wave were randomly distributed, as occurs in natural light sources. The repeating temporal coherence of a laser diode source can be characterized by the coherence interval (l_i), which represents the distance along the beam at which it has the same state of coherence.

Because in most interferometric applications, including ESPI, the optical path differences across the interfering wavefronts can be large [7], a significant temporal coherence is required. This forces high-coherence lasers as the only possible choice for illumination sources in conventional ESPI setups. Such single-frequency lasers have been designed to suppress all but one longitudinal mode, which leads to very small bandwidth and consequently long coherence length. The coherence requirements for in-plane ESPI are quantitatively investigated in the next section.

4.2 Coherence requirements for in-plane strain measurements

The requirement for significant coherence length in in-plane ESPI is mainly due to the presence of oblique illumination angles, as illustrated in Figure 4.3. In the upper path ray *b* travels a greater distance than ray *a*. The same is true in the lower path for rays *B* and *A*, respectively. In the case of symmetric illumination, the corresponding path length differences are:

$$OPD_{ab} = OPL_b - OPL_a = Dtan(\theta), \tag{4.2}$$

$$OPD_{AB} = OPL_B - OPL_A = Dtan(\theta), \tag{4.3}$$

where *D* is the diameter of the collimated laser beam. The path length differences are illustrated using dashed blue lines. The beams overlap on the object surface – *a* overlaps with *B* and *A* overlaps with *b*. Consider a case where the geometry is adjusted so that the path length difference at the upper edge of the illuminated area is zero:

$$OPD_{aB} = 0. \tag{4.4}$$

Based on the geometry, the path length difference at the lower edge is then:

$$OPD_{Ab} = OPD_{ab} + OPD_{AB} = 2Dtan(\theta). \tag{4.5}$$

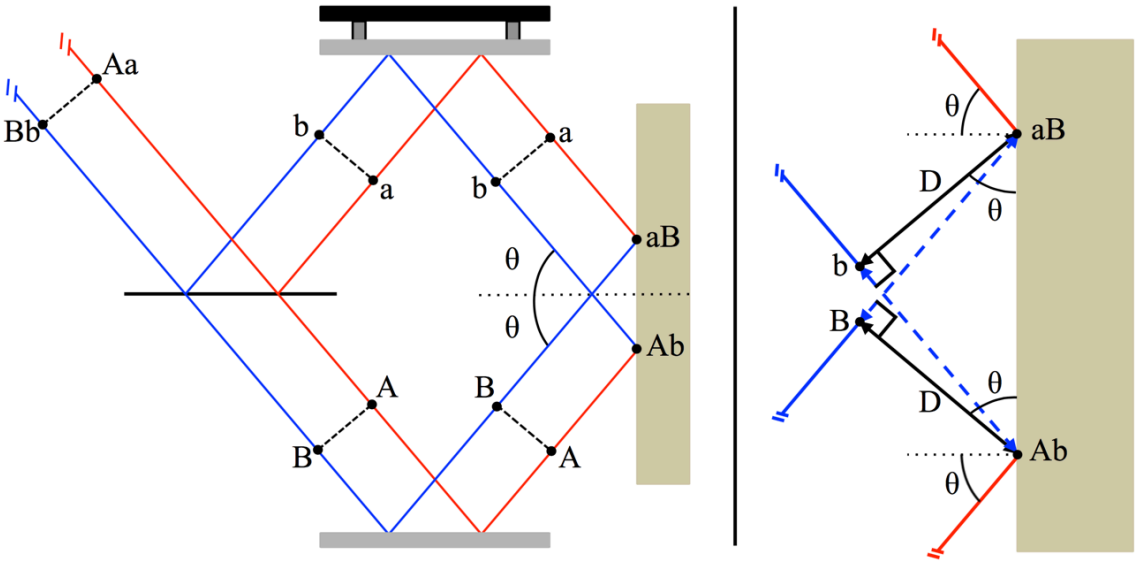

Figure 4.3 *Illustration of the path length differences across the illuminated area due to oblique illumination angles.*

The path length difference between the interfering beams changes linearly across the illuminated area. If the OPD for the central parts of the beams were minimized to zero, then the maximum variations would be $\pm Dtan(\theta)$. For example, in a case of 40 mm wide beams illuminating the object at 45° angles, the maximum differences in path lengths would be ±48 mm. This variation is more than a magnitude higher than the coherence length of typical laser diodes. If low coherence length laser light were used, the illuminated area would consist of vertical bands of high coherence, separated by a distance dependent on the coherence interval of the laser source. The width of the coherence bands is related to the laser's coherence length. The areas between the bands suffer from low modulation (visibility).

In ESPI the degree of coherence and thus the measurement quality can be investigated by calculating and mapping the intensity modulation for each pixel. Intensity modulation is often called fringe visibility (V), and in the case of four-step phase stepping it has a form [41]:

$$V = \frac{2\sqrt{(I_1 - I_3)^2 + (I_4 - I_2)^2}}{I_1 + I_2 + I_3 + I_4}. \tag{4.6}$$

Possible visibility values range from 0 to 1, from no to full visibility, respectively. In experimental setups the visibility values close to unity are impossible to achieve due to the presence of noise. Figure 4.4 shows an example of the visibility map measured with an in-plane interferometer using low-coherence laser. The visibility values are displayed for each pixel in gray-scale. The plotted red line represents the column averages, and is scaled to the color bar values.

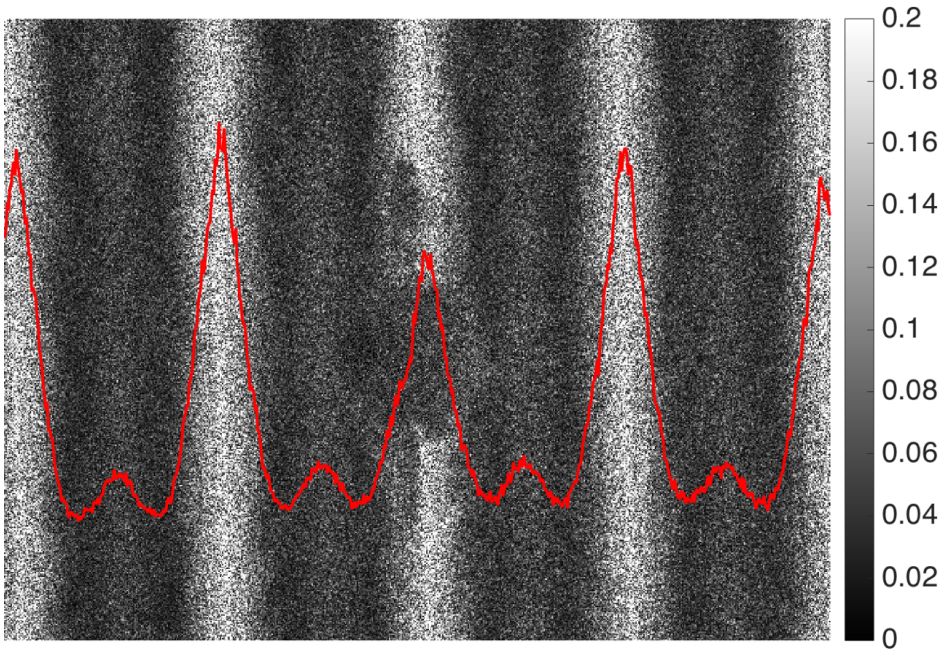

Figure 4.4 *An example of a visibility map for in-plane ESPI measurement using laser with a low coherence length.*

It is clear that a measurement system with such nonuniform performance as shown in Figure 4.4 could not be used for full field displacement and strain measurements. The coherence requirements should be somehow relaxed in order to achieve uniform measurement quality with laser diodes. This is possible with diffraction gratings, which will be discussed in the following sections.

4.3 Operation of diffraction gratings

A diffraction grating is an optical component that has a series of uniformly spaced grooves formed on a glass or film substrate. The separation of individual grooves is in the order of the wavelength of light used [48]. Grooves split and diffract the incoming light wave. In a transmission grating, the diffracted light is transmitted through the grooves. In a reflection grating, on the other hand, the surface of the substrate is coated with reflective material, reflecting the diffracted light at the grating surface. The common groove profiles include sinusoidal, square and sawtooth step patterns.

When monochromatic light is incident on a grating surface, it is diffracted into discrete angles [46]. This occurs because light rays diffracted at each groove interfere with one another and the occurring interference is constructive only at certain directions, diffraction orders, depending on the grating properties and the wavelength of the light used.

Figure 4.5 illustrates the behaviour of light incident on the surface of a ruled reflection diffraction grating. The incident light is diffracted into different diffraction orders (m). The diffraction angle depends on the incidence angle θ_i, the light wavelength λ and

groove separation d_g. The diffraction angles can be calculated from the grating equation [48]:

$$d_g(\sin(\theta_m) + \sin(\theta_i)) = m\lambda. \tag{4.7}$$

The angles are taken with respect to the grating surface normal. Angles are positive on the side of the incident light. For reflection gratings the diffraction order $m = 0$ corresponds to specular reflection from the grating surface. For normal incidence ($\theta_i = 0°$) the diffraction equation reduces to familiar form:

$$d_g \sin(\theta_m) = m\lambda. \tag{4.8}$$

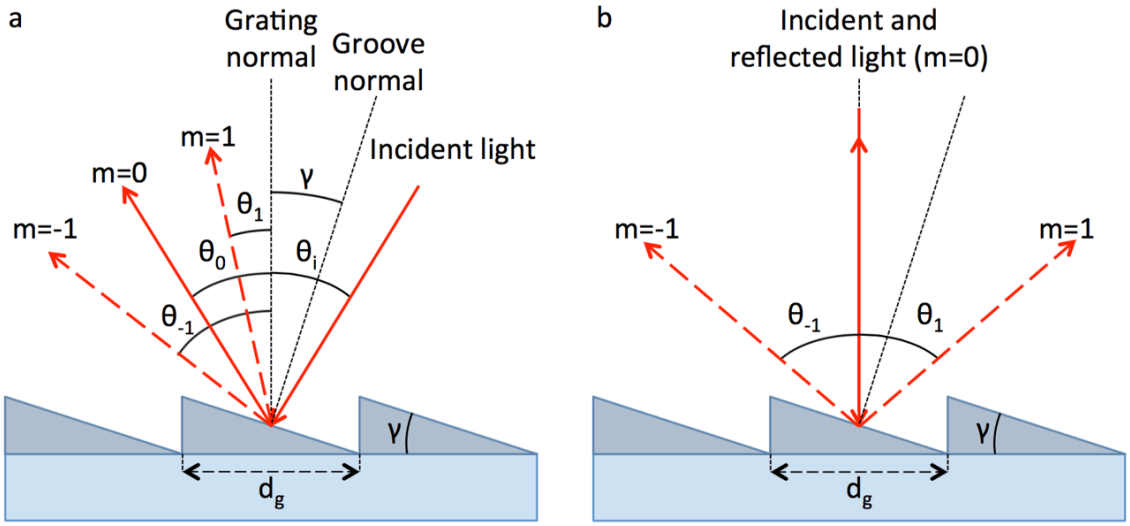

Figure 4.5 *Diffraction at a surface of a ruled reflection diffraction grating. (a) General case, (b) normal incidence.*

In ruled diffraction gratings with a sawtooth profile the groove angle γ does not affect the diffraction angles but, however, it has a substantial effect on the diffraction efficiency. The optical power diffracted into a diffraction order m is maximized when the groove normal bisects the angle between the incident light and the light diffracted into m^{th} diffraction order [46]:

$$\gamma = \frac{\theta_i + \theta_m}{2}. \tag{4.9}$$

In this situation the angle of diffraction coincides with the specular reflection from the groove surface. Combining equations (4.7) and (4.9) leads to:

$$\lambda_B = \frac{2d_g}{m}\sin(\gamma)\cos(\gamma - \theta_i), \tag{4.10}$$

where λ_B is the wavelength that fulfills the condition, and is called the blaze wavelength. For other wavelengths the diffraction efficiency is smaller. Equation (4.10) shows that the blaze wavelength depends on the system configuration. For given grating specifications the blaze wavelength is largest when the incident angle is equal with the blaze angle. In such a case the diffraction angle is also equal with the incident angle and the beam directed towards the grating returns on the same path. This specific arrangement is known as Littrow configuration that is widely used for various applications, including monochromators for laser tuning and spectrographs for spectroscopy [48]. Diffraction grating efficiencies are typically specified for Littrow configuration.

4.4 Path length compensation using a diffraction grating

Figure 4.6 shows an ESPI setup where a reflection diffraction grating has been added between the collimating lens (not shown) and the beam splitter. The diffraction grating cuts the incoming wavefronts. As shown in the figure, a significant portion of the light rays diffract into an angle θ, corresponding to a diffraction order $m = 1$. Some light diffracts back towards the collimating lens (diffraction order $m = 0$) and some diffracts into an angle $-\theta$ (diffraction order $m = -1$). Higher order diffractions may be possible depending on the grating dimensions but are not considered here.

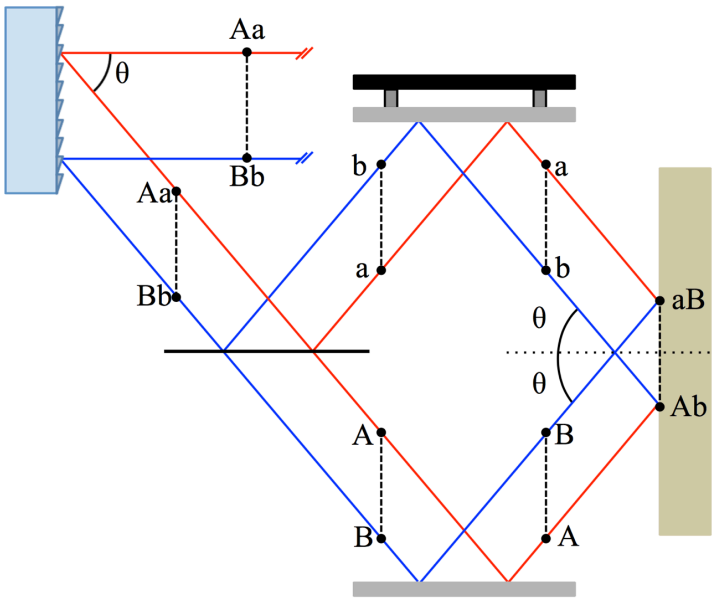

Figure 4.6 *Path length compensation in in-plane ESPI using a ruled reflection diffraction grating.*

Diffraction causes a path length difference across the diffracted beam. The dashed lines represent wave "timefronts," i.e. rays that have travelled the same duration and thus the same distance from the source. When the angle between the incident and diffracted beams $\theta = \theta_i + \theta_1$ is adjusted equal to the illumination angle, the path lengths across the entire beam become equal. Diffraction grating can thus compensate for the path length

differences due to oblique illumination and help to relax the temporal coherence requirements in ESPI.

ESPI systems based on a combination of a laser diode and a diffraction grating have been already demonstrated by Viotti and Albertazzi [49], and by Schajer et. al. [27]. Both of these realizations were based on a transmission type grating. Transmission diffraction gratings are attractive because a beam splitter is not required in the ESPI setup. The diffracted beam of order $m = 1$ starts one interferometer path, while the beam of order $m = -1$ starts the other path. However, a major disadvantage of transmission gratings suitable for ESPI is their low efficiency. This is due to two factors. First, the diffracted power at diffraction orders $m = 1$ and $m = -1$ should be equal; otherwise the fringe contrast would be reduced [28]. Thus, the sawtooth groove profile is not suitable, and blaze-angle based optimization cannot be used. This is partly overcome by the fact that both diffraction orders $m = \pm 1$ are utilized, unlike with the solution based on the reflection grating. The second, more serious matter is the required amount of path length optimization. In ESPI the practical illumination angles around 45° require considerably high groove densities in order to achieve equal diffraction angles. At high densities, however, the efficiency of transmission gratings at visible range drops due to the limitations in refractive properties of grating materials [50]. This is what makes the path length compensation using ruled reflection gratings an attractive, potential alternative.

5. EXPERIMENTAL DESIGN AND VALIDATION

The chapter begins by describing how a synthetic fringe pattern was created and what it was used for. Then the details of the different experimental setups used are introduced. Finally, the implementation of the proposed strain calculation algorithm is explained.

5.1 Synthetic data

A synthetic wrapped fringe pattern was created in order to study the characteristics, effectiveness and accuracy of the proposed strain calculation algorithm. Synthetic data removes uncertainties associated with experimental data and allows detecting potential limitations and errors caused by data processing steps. Hence, it is a useful tool in validation of the proposed strain calculation algorithm. The strain in the generated pattern increases linearly from zero at the left edge to a value 0.75 rad/pixel at three quarters of the total width from the left. After this, strain decreases linearly back to zero at the right edge. In order to study the preservation of details and the level of spatial resolution, a square of zero phase and thus zero strain was added. The interface between the square and its surroundings has sharp phase jumps. Normally distributed numerical noise with zero mean and standard deviation = 1.1 was added to the generated pattern to simulate measurement noise. The level of noise was adjusted to be comparable with the noise levels found in experimental data. The introduced noise reduces fringe contrast, making the phase jumps barely visible especially at the strain concentration areas where fringe density is highest.

5.2 High-coherence measurement setup

High-coherence ESPI data were recorded using a setup geometry shown in Figure 2.2. The illumination source was a 632 nm, 50 mW diode-pumped solid-state (DPSS) laser (JDS Uniphase). The laser output was diverged using a convex lens integrated to laser housing and subsequently collimated using a plano-convex lens. The collimated laser beam was divided into two paths using a non-polarizing 50/50 beam splitter plate (Thorlabs EBS2, diameter = 50 mm). The transmitted and reflected beams were steered using a fixed and piezo mirror, respectively. The mirrors were front-surface coated. The fixed mirror was attached to a precision translation stage equipped with a two-axis tilt mount. The other mirror was attached to four piezoelectric transducers (Thorlabs TA0505D024W, one in each mirror corner) connected in parallel. The mirrors were carefully placed and oriented so that the two interferometer arms had symmetric paths with equal path lengths and that illuminating light beams overlapped at the specimen

surface. The specimen was illuminated symmetrically at 50° angles with respect to the object surface normal.

The test object was a rectangular nylon specimen (120 x 98 x 25 mm^3). A 6mm through-hole was drilled and two vertical cracks sawn in order to cause larger strain concentrations under loading. A thin layer of matt white paint was sprayed on the surface to increase reflectance. The object was fixed to the optical table and loaded compressively at the sides, i.e. in horizontal direction, parallel to the measurement sensitivity direction.

The speckle pattern reflected from the object surface was captured using a monochromatic machine vision style digital camera (ProSilica EC750). The camera resolution was 640x480 and pixel size 6x6 μm^2. The camera module was attached to a macro lens (Navitar zoom 7000, focal length = 18–108 mm) with controllable magnification ratio and aperture size. Magnification ratio of 0.12 was used in the measurements, so each pixel in the image plane corresponded to 50 μm on the object surface. The in-plane displacements can be calculated from the measured phase map using equation (3.5). For high-coherence measurements the displacement–phase relation was 55 nm/rad.

Helios program, developed by Professor Gary Schajer, was used for calibrating the phase stepping and recording the measurement data. The phase stepping calibration procedure iteratively adjusts the voltage applied to PZT elements and monitors the resulting phase step to obtain the required 90° step angle. In the actual measurement the program records four phase-shifted reference images of the speckle pattern. The object is then deformed by a static compression from the sides, and another set of four phase-stepped images is recorded. When a reference set is saved, the wrapped phase map due to deformation can be monitored on a screen in real time. The software also calculates and displays the phase step angle for each measurement set. On the course of measurements, the step angle was monitored and the PZT voltage calibrated when needed. Finally, the measured data sets were exported for post-processing in Matlab. Each dataset contained four reference frames and four deformed frames, each in a TIFF-image format.

5.3 Low-coherence measurement setup

The novel ESPI setup based on a laser diode and a reflective diffraction grating is shown in Figure 5.1. The illumination source was a 638 nm, 110 mW single transverse mode laser diode (Mitsubishi ML520G54). The diode was operated at around 50 mW using an in-house built current driver. The coherence length of this diode had been earlier investigated to be 1.55 mm [51].

The beam from the laser diode was first expanded and collimated. The collimated laser beam was then directed on the reflection diffraction grating (Thorlabs GR50-1205), where the light rays were diffracted and reflected. The angle of incidence was parallel to the grating surface normal. The blaze angles of grating grooves were 17.45° and groove density 1200 grooves/mm. At 638 nm, the reflection grating had an efficiency of 60% [52], while a comparable transmission grating (Thorlabs GT50-12) had an efficiency of only 17% [53]. Using equation (4.8), the calculated diffraction angle for the setup was determined to be 50.0°. The illumination angles were consequently set to 50.0° in order to obtain ideal path length compensation. The rest of the interferometer geometry was identical with the high-coherence ESPI setup introduced above.

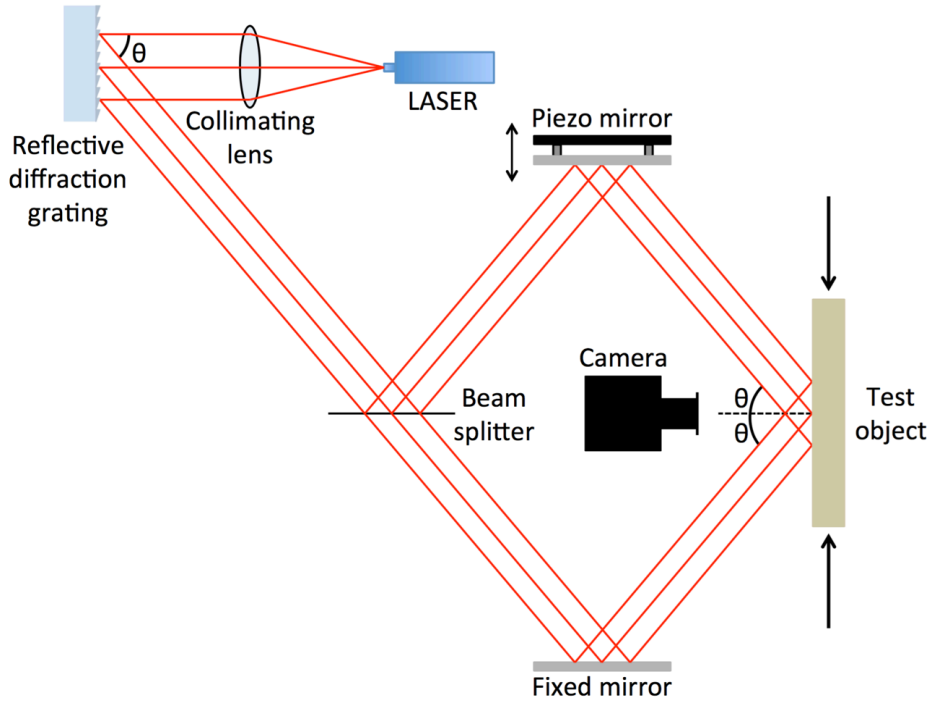

Figure 5.1 *Novel ESPI measurement setup based on a red laser diode and a reflective diffraction grating.*

Because the laser diode wavelength was different from the wavelength of the high-coherence laser, the speckle size was changed. Hence, the camera objective aperture size was slightly altered to match the speckle size with pixel size. For low-coherence measurements the displacement–phase relation was 66 nm/rad. The magnification ratio was kept unchanged from the high-coherence measurements. For comparison, measurements without the diffraction grating were also taken. The diffraction grating was replaced with a conventional front-surface mirror but rest of the setup was unchanged. The data acquisition was performed using Helios in the same way as with the high-coherence measurements.

5.4 Strain calculation algorithm implementation

All post processing of the data was done in Matlab. The TIFF-image files created in Helios were first imported to Matlab and changed to double-precision format. The phase map was calculated from the image files using equation (2.17). The phase map was then transformed to phasor format using equation (2.18), and zero-modulation pixels were excluded. A mask was created for the area containing the hole and slits. The pixels within the mask were set as complex zeroes so that they would not affect the results.

The repetitive filtering of the phase map was performed using Matlab's conv2-function. As a standard inbuilt function it is optimized by vectorization and thus much faster compared to solutions based on nested loops. The filtering kernel was similar to the one shown in equation (3.4). The specification parameter 'same' was used in conv2 function so that the filtered image had the same dimensions as the input image. The filtered image was renormalized, potential new zero-modulation pixels eliminated and re-masking performed. This procedure was repeated for a specified number of times.

A phasor format strain map for principal strain component ε_{xx} was calculated from the filtered, wrapped phase map using equation (3.9) and a chosen gauge length. The strain map is $2K$ pixels narrower than the phase map due to central difference strain calculation. The calculated strain field was repetitively filtered in the same way as the phase map, but using different parameter values. The strain map was obtained by calculating the argument, i.e. the angle, of the filtered strain phasors. Finally, the map of the strain angles was scaled using the phase-displacement relation and the physical width of the pixels. The obtained phase and strain maps were then displayed and saved as image files.

6. RESULTS AND DISCUSSION

The chapter begins by investigating the optimal phase filtering parameters for experimental data. The effects of gauge length, filtering kernel size and number of repetitions are studied using the generated synthetic data. Then, the performance of the algorithm is studied using high-coherence data at different loading levels. A similar set of data is recorded using the novel low-coherence ESPI setup, and the measurement quality of the different setups are compared. Measurement range is then discussed, followed by a comparison of the performance and characteristics between the developed algorithm and other existing methods.

6.1 Optimal phase filtering parameters

Experimental ESPI data was first recorded using the high-coherence setup. The recorded phase map and a comparison of different phase filtering parameters are shown in Figure 6.1. The measurement object was under heavy compressive loading, so the phase pattern has high fringe density and substantial level of noise due to speckle decorrelation. The high noise level significantly reduces fringe contrast and makes direct strain calculation impossible. Mean filtering using a large 11x11 kernel has good performance at areas where the fringe density is modest. However, at areas of largest phase gradients around the slits the use of the large kernel leads to serious phase distortion, rendering the data unusable. On the other hand, mean filtering with a small 3x3 kernel avoids phase distortion but leaves significant level of residual noise. When the 3x3 mean filtering is repeated multiple times, the level of residual noise is reduced. When the number of repetitions is set to 15 or 25, the majority of the phase map is extremely smooth. However, distortions occur at the areas closest to slit tips, corresponding to locations of high strains. In addition, some singularity points exist, where the phase jump contour line has a discontinuity. In order to limit the expansion of these error areas, the number of filtering repetitions should be limited. Thus, the 3x3 kernel applied five times was found optimal for the experimental data. The filtering errors are contained in the very small area around the masked region. On the other hand, some residual noise is left, and subsequent strain data filtering is necessary.

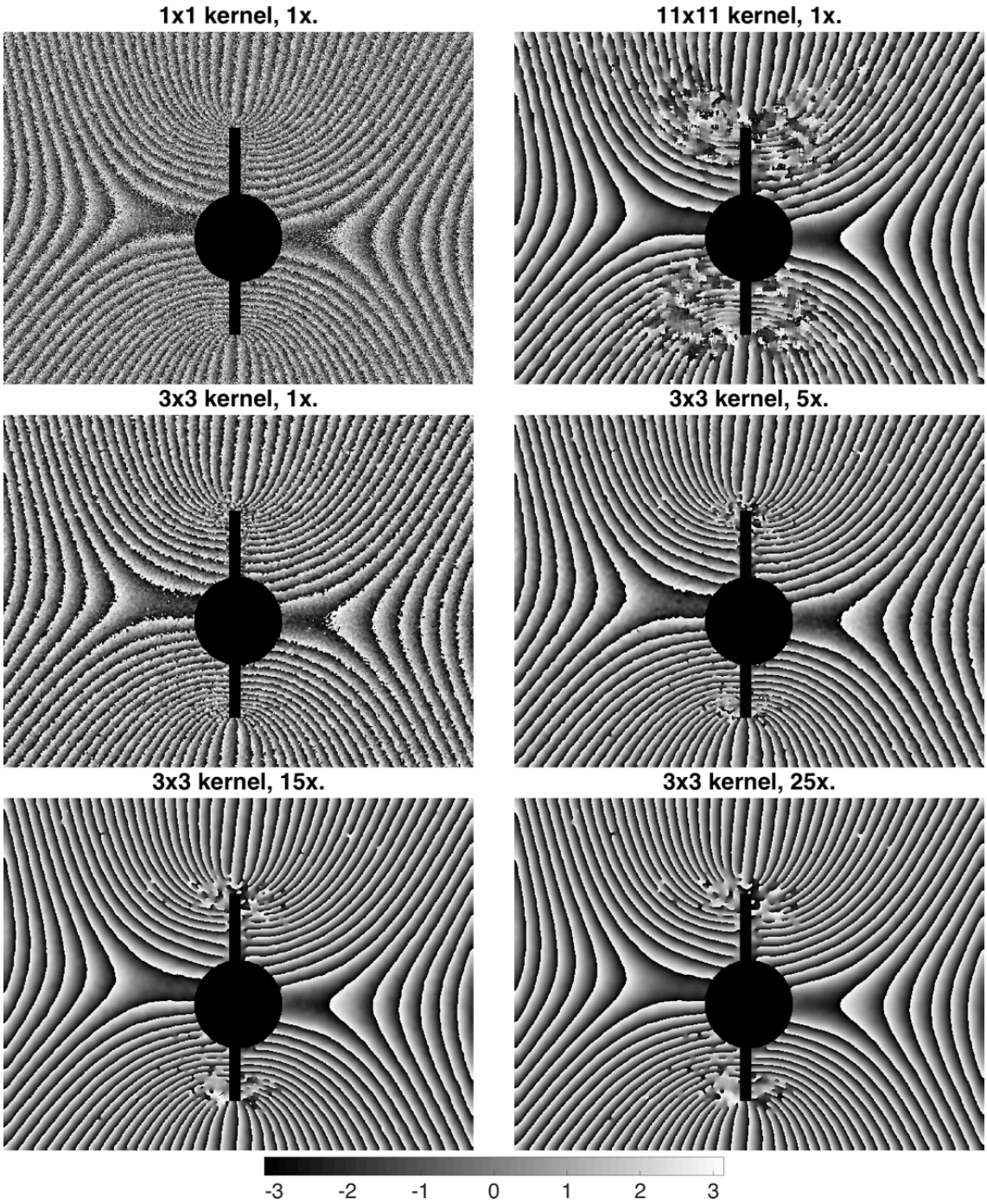

Figure 6.1 *Comparison of different phase filtering parameters. The hole and slits on the imaged area have been masked and are displayed in black. Phase values are displayed in radians.*

6.2 Synthetic data results

Figure 6.2 shows the generated synthetic phase pattern first without noise, with added simulated noise and after a repetitive mean filtering using a 3x3 kernel and five repetitions. The corresponding calculated strain maps show the effect of noise on the quality of strain field evaluation. The true strain increases and decreases linearly except

for the interfaces around the added zero strain area due to phase discontinuities. The strain map calculated from the noisy synthetic phase pattern without any filtering illustrates well the noise amplification phenomenon. The strain distribution is completely overshadowed by noise, which means that filtering is unquestionably required.

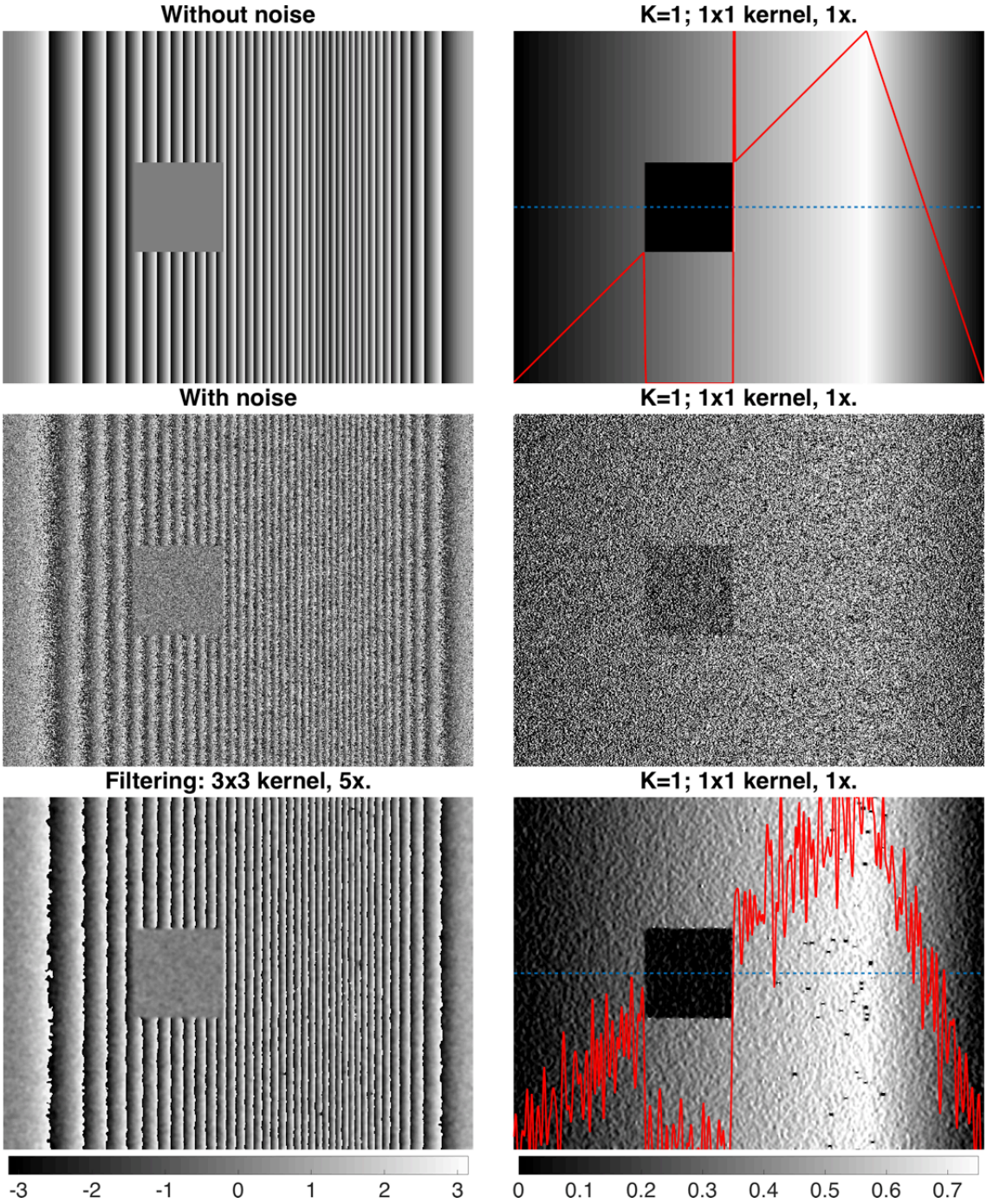

Figure 6.2 *The generated synthetic phase pattern (left column) and the corresponding calculated strain field (right column). Top row: without noise; middle row: with simulated noise; bottom row: the noisy data after phase filtering. The solid red line is a plot of strain along the dashed blue line in the middle. The plot is omitted for the center row for clarity. Phase unit is radian and the unit of strain is rad/pixel.*

The repetitive filtering of the phase pattern dramatically improves the contrast of the calculated strain field. However, some notable residual noise is present, which appears as grainy texture in the strain map. The true peak strain in the synthetic strain map is 0.75 rad/pixel. Using the phasor format central difference strain calculation, the extreme strain values are limited by the gauge length. For values K=1, 2 and 3 these limits are $\pm\pi/2$, $\pm\pi/4$ and $\pm\pi/6$, respectively. If the local strain exceeds this value, it becomes wrapped. High noise level makes data prone to wrapping errors, especially within areas of high strains. In Figure 6.2 some wrapping errors are present near the strain peak, which appear as black dots corresponding to negative strain values.

Figure 6.3 shows a comparison of gauge lengths K=2 and K=3 used in strain calculation applied on the same filtered data shown in Figure 6.2. When compared with the case K=1, the gauge length K=2 has some additional wrapping errors. However, with the gauge length K=3 the wrapping effects are much more adverse. On the other hand, at the areas of lower strains the level of noise reduces with increasing K. This can be seen as the grainy texture becoming smoother and as reduced variations in the plotted line graphs. Over a longer gauge length the true phase gradient is higher, while the level of noise is constant. This improves the SNR in the strain calculation. Unfortunately, the limit for peak strain is smaller for longer gauge lengths. Consequently, a large value of K limits the calculable strain range. The highest fringe density in the synthetic phase pattern is very high compared to typical experimental measurements. Still, the value of K has to be limited even with experimental data, because high level of noise may lead to wrapping errors even if the true strain would not exceed the limit for the given gauge length. Hence, the gauge length K=1 is chosen to be used from here onwards.

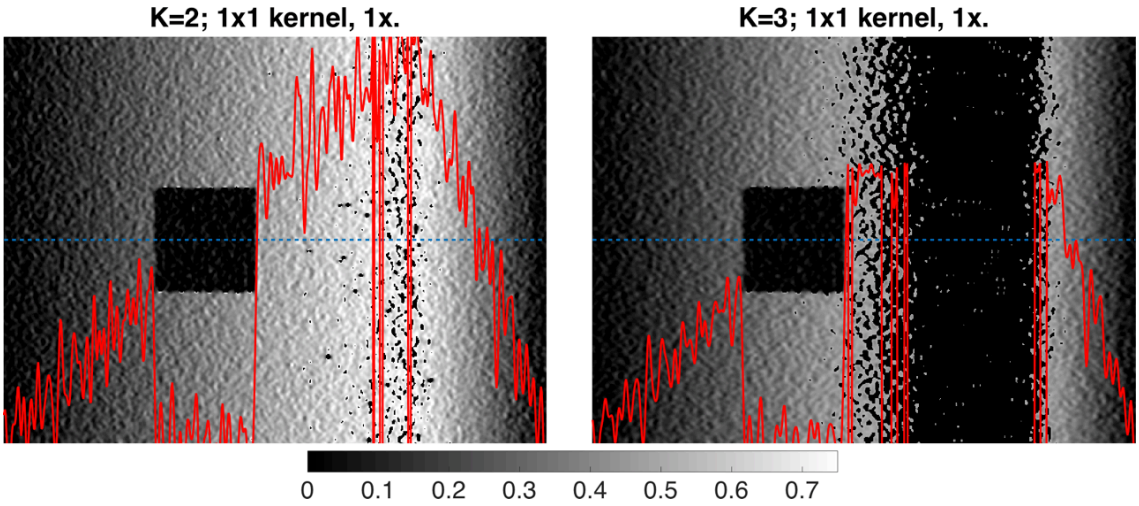

Figure 6.3 *The strain field calculated from the filtered phase pattern using gauge lengths K=1 (left) and K=2 (right).*

The residual noise in the strain field has to be filtered away. The repetitive strain field filtering was investigated using kernel sizes 3x3, 9x9 and 15x15. The numbers of iterations used were 1, 5, 10 and 15. The filtering results are shown in Figure 6.4.

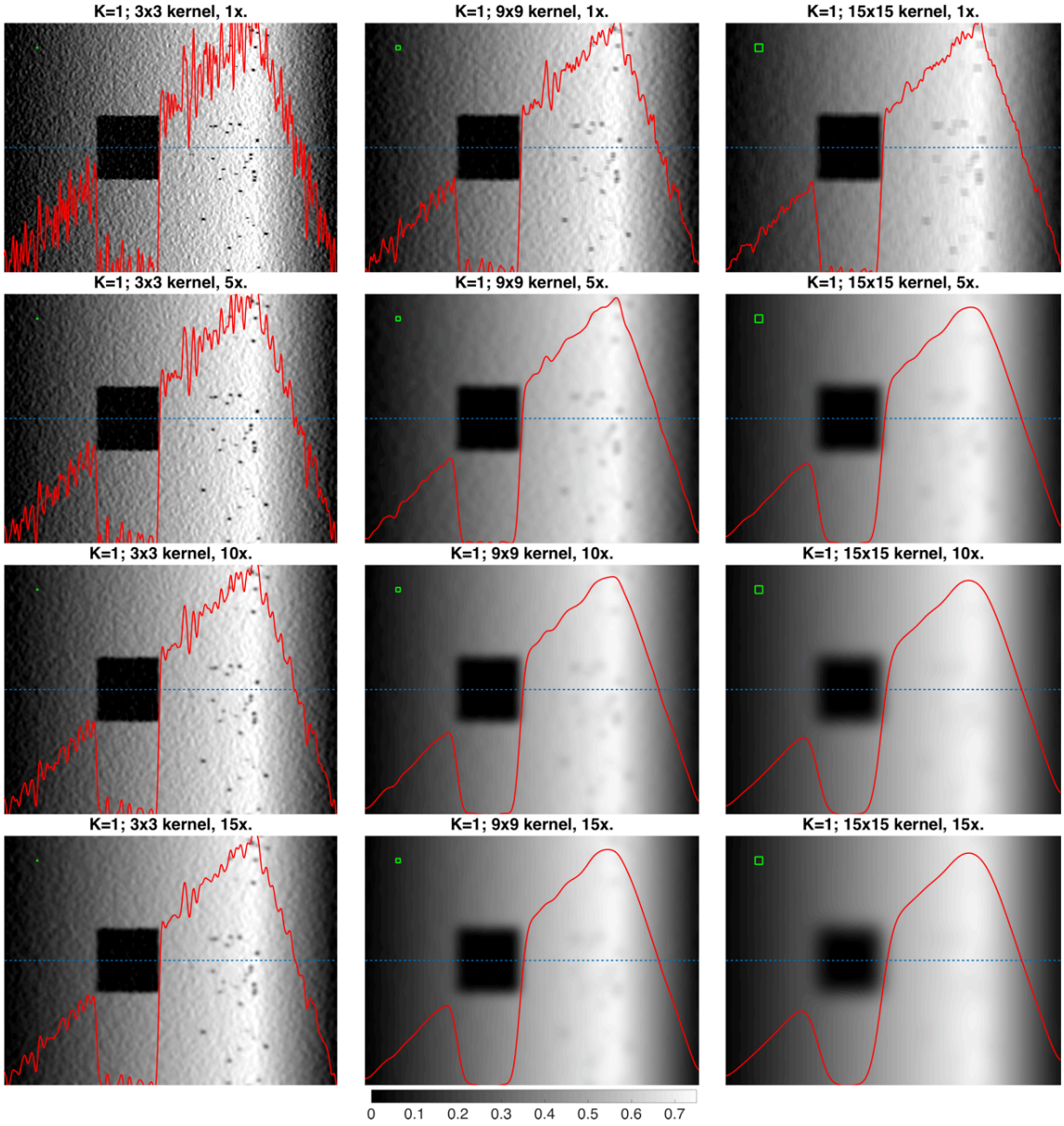

Figure 6.4 *Comparison of different repetitive strain filtering parameters applied to the filtered phase pattern shown in Figure 6.2. From top to bottom, the numbers of repetitions in each row are 1, 5, 10 and 15. From left to right, the kernel sizes in each column are 3x3, 9x9 and 15x15. The solid red line is a plot of strain along the dashed blue line in the middle. The green squares show the filtering kernel sizes.*

Increasing the kernel size and the number of iterations both increased the filtering effect. With the 3x3 kernel the level of residual noise after filtering is significant even after 15 repetitions. In addition, the wrapping errors are clearly present. It was found that even higher numbers of repetitions did not improve the situation. With 9x9 and 15x15 kernels the filtered strain field is smoother, which is logical thanks to a greater averaging effect. On the other hand, the increasing smoothness in general reduces the

spatial resolution. This can be seen by monitoring the edges of the square zero-strain pattern and the corresponding part of the line graph. The sharp discontinuities become blurred when the number of repetitions and kernel size are very high. The 9x9 kernel at ten repetitions was found to be the optimal filtering combination for the synthetic data. The overall smoothness of the strain field is very good and the few wrapping errors are filtered relatively well. Some slight blurring in the square edges occurs, but it is not excessive as with the highest filtering parameters.

6.3 High-coherence data results

A set of experimental phase fringe patterns was recorded using the high-coherence setup by compressively loading the slit-hole nylon specimen at different loading levels. Figure 6.5 shows the filtered phase maps and the corresponding filtered strain fields for the principal strain ε_{xx} at four different loading levels (HC1…HC4). A minimum gauge length K=1 was used. Using a common sign convention, compressive strain is marked negative and tensile strain positive. The numbers of filtering repetitions were five for the phase maps and ten for the strain maps. The kernel sizes were 3x3 for the phase maps and 9x9 for the strain maps.

At the lowest loading level HC1 the filtered phase map was very smooth and no filtering errors were present. Consequently, the calculated and filtered strain field was also smooth. The phase pattern corresponding to the second loading level HC2 was the same that was used for the filtering parameter comparison in Figure 6.1. The higher loading lead to higher fringe density and higher level of noise. Fringe distortion and some single errors were well contained and the overall data quality was good. The corresponding strain field had higher peak strains than in HC1. When the loading was further increased in HC3, the distorted area around the slits grew and covered a larger area. The number of phase singularity points also increased. However, the strain field was still reasonably well defined, although some spots caused by phase singularities were present. At the highest loading level HC4 the noise was clearly dominating and causing filtering errors that corrupted the phase field. Consequently, the determined strain field was no longer well representing. The maximum resolvable compressive strains were 723 microstrain (strain x10^{-6}, or μm/m) in HC3 and 744 microstrain in HC4.

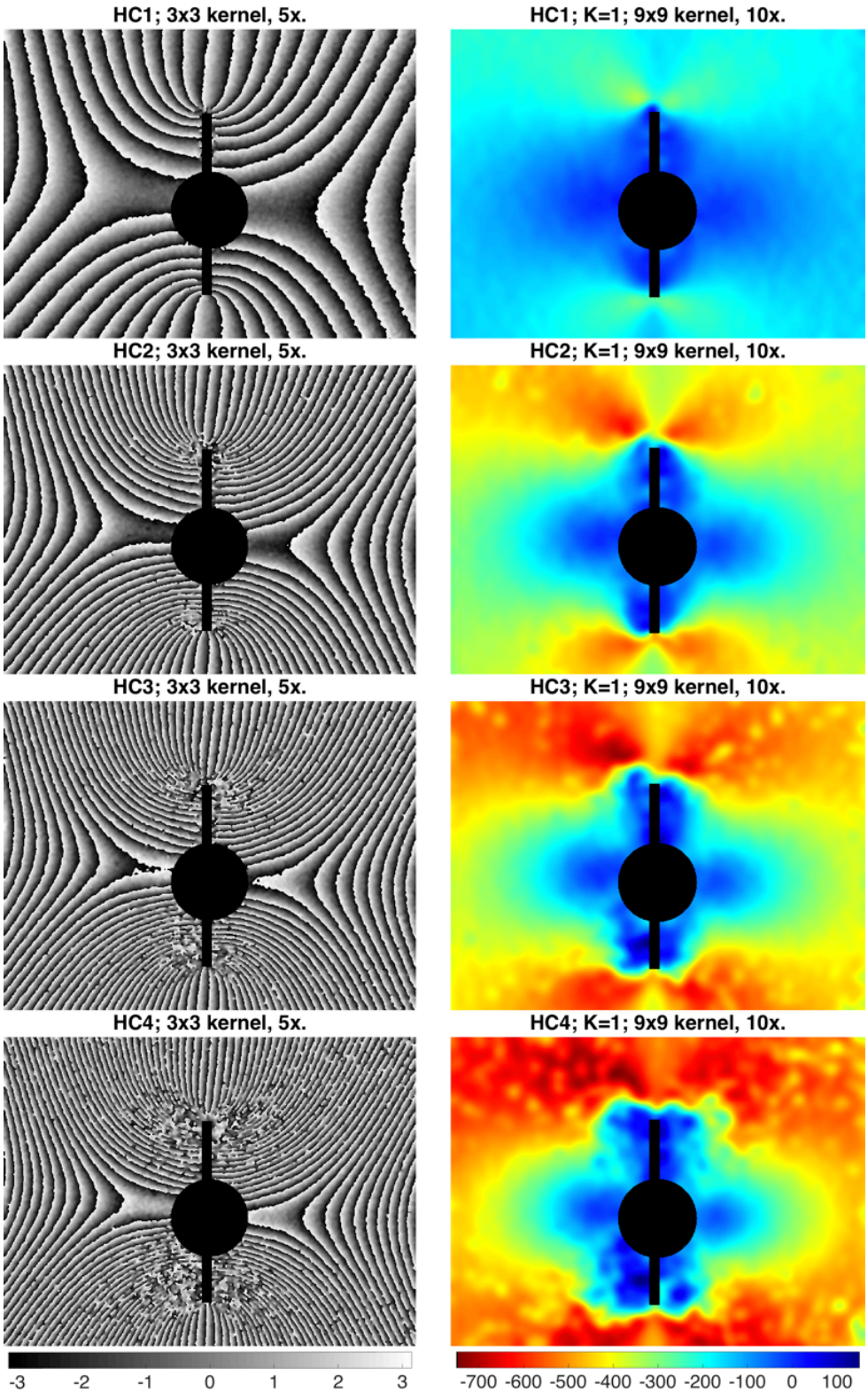

Figure 6.5 *Filtered high-coherence phase patterns (left column) and corresponding calculated strain fields (right column) at different loading levels. The applied compressive loading level increases from top to bottom. Phase is shown in radians and the unit of strain is microstrain (strain x10^{-6}).*

It was found that five repetitions of phase filtering lead to best results independent of the loading level. At the lowest loading HC1 five repetitions produced a uniformly smooth phase pattern. The level of residual noise depended on the load when loading was further increased. The phase distortions caused by the higher loading levels were reasonably well contained in the vicinity of the slits especially for the case HC2. Resolving the strains closest to slits was impossible due to overwhelmingly high levels of speckle decorrelation noise. However, the areas of highest distortions in HC3 and HC4 seemed not exactly coincide with the locations of the strain peaks seen in HC1 and HC2. It is important to remember that the displacement and strain sensitivity was solely in the horizontal direction. Nevertheless, in reality there were displacements and strains also in the vertical direction. This is explainable by the Poisson's effect: compressive strains along one axis cause tensile strains along the axes normal to it. The phenomenon becomes intuitive if one thinks how a sponge or dough behaves when it is pressed or stretched. While there was no displacement sensitivity in the vertical direction, speckle decorrelation was understandably affected by also the vertical movements. Hence, it is reasonable to expect that significant y-displacements at the most distorted areas must have occurred.

High decorrelation noise in combination with high fringe density ultimately limits the maximum strains that can be resolved. At the highest loadings, small number of phase filtering repetitions would not remove enough noise, while too many repetitions would lead to severe spreading of the highly distorted areas. In the strain maps the filtering must also be limited in order to maintain good spatial resolution.

The effect of the gauge length was also studied with experimental data. Figure 6.6 shows the loading case HC3 but here calculated using gauge lengths K=2 and K=3. With K=2 the results seem similar but the peak strains have been rounded down. In addition, the strain deviations caused by phase singularities covered larger areas. These effects are understandable; longer gauge leads to higher averaging, which affects especially the extreme values. The longer gauge has also a longer reach, so the effect of a single faulty pixel extends to a wider area.

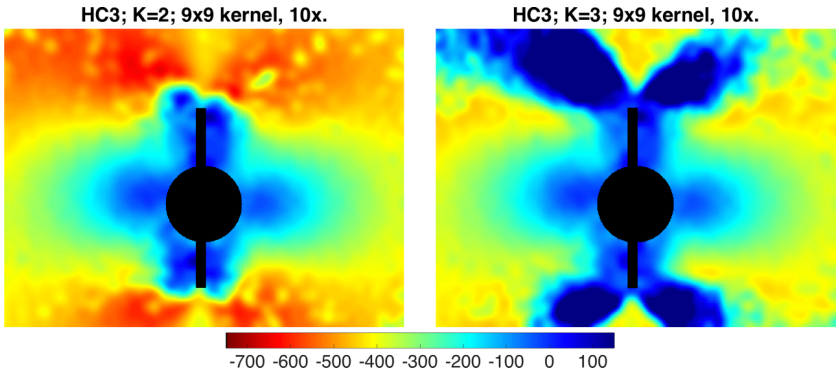

Figure 6.6 *Gauge length comparison. The unit of strain is microstrain (strain x10^{-6}).*

When the gauge length was further increased to value K=3 the consequences were dramatic. Wrapping effects dominated and distorted the important peak strain areas. Areas of highest compressive strains falsely appear to have large tensile strains. The findings support the conclusions made from the synthetic data; the gauge length should be limited and the smallest value K=1 should be used in the presence of high strains.

6.4 Low-coherence data results

After the high-coherence measurements the green DPSS laser source was replaced with the red low-coherence laser diode and the system was realigned. The performance of the low-coherence setup was first studied without path length compensation. The corresponding results are shown in Figure 6.7. The phase map had alternating bands of higher and lower quality, respectively. The fringes in low-quality regions were barely visible. In the filtered phase map the higher quality areas had very smooth phases, while the fringes in low quality areas were severely smeared. In addition, the interfaces between the higher and the lower quality bands showed distortion. The calculated strain map was consequently affected by distortions and discontinuities and contained little useful information.

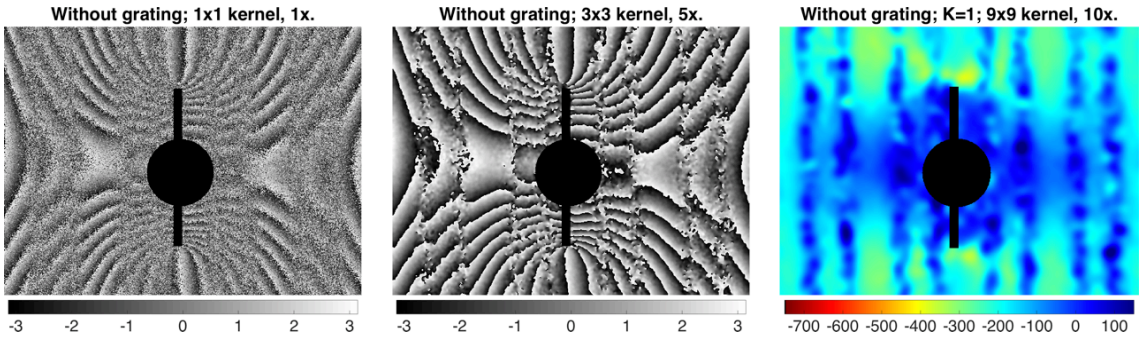

Figure 6.7 *Low-coherence ESPI measurement results without path length compensation. The phase pattern consists of repeating bands of higher and lower quality. Left: Phase pattern before filtering; center: filtered phase pattern; right: strain field calculated from the filtered phase pattern. Phase is shown in radians and the unit of strain is microstrain (strain x10^{-6}).*

The discontinuities in the data are explainable by the low coherence length of the laser diode and the linearly changing path length differences across the measurement region. In the high quality bands the path length differences have been within the coherence length of the laser diode. Correspondingly, the low quality bands have suffered from low coherence.

Next, the diffraction grating was added into the setup for path length compensation, and the system was realigned. A set of measurements was taken at four different loading

levels (LC1…LC4) in the same way as with the high-coherence setup. The obtained filtered phase patterns and corresponding filtered strain maps are shown in Figure 6.8.

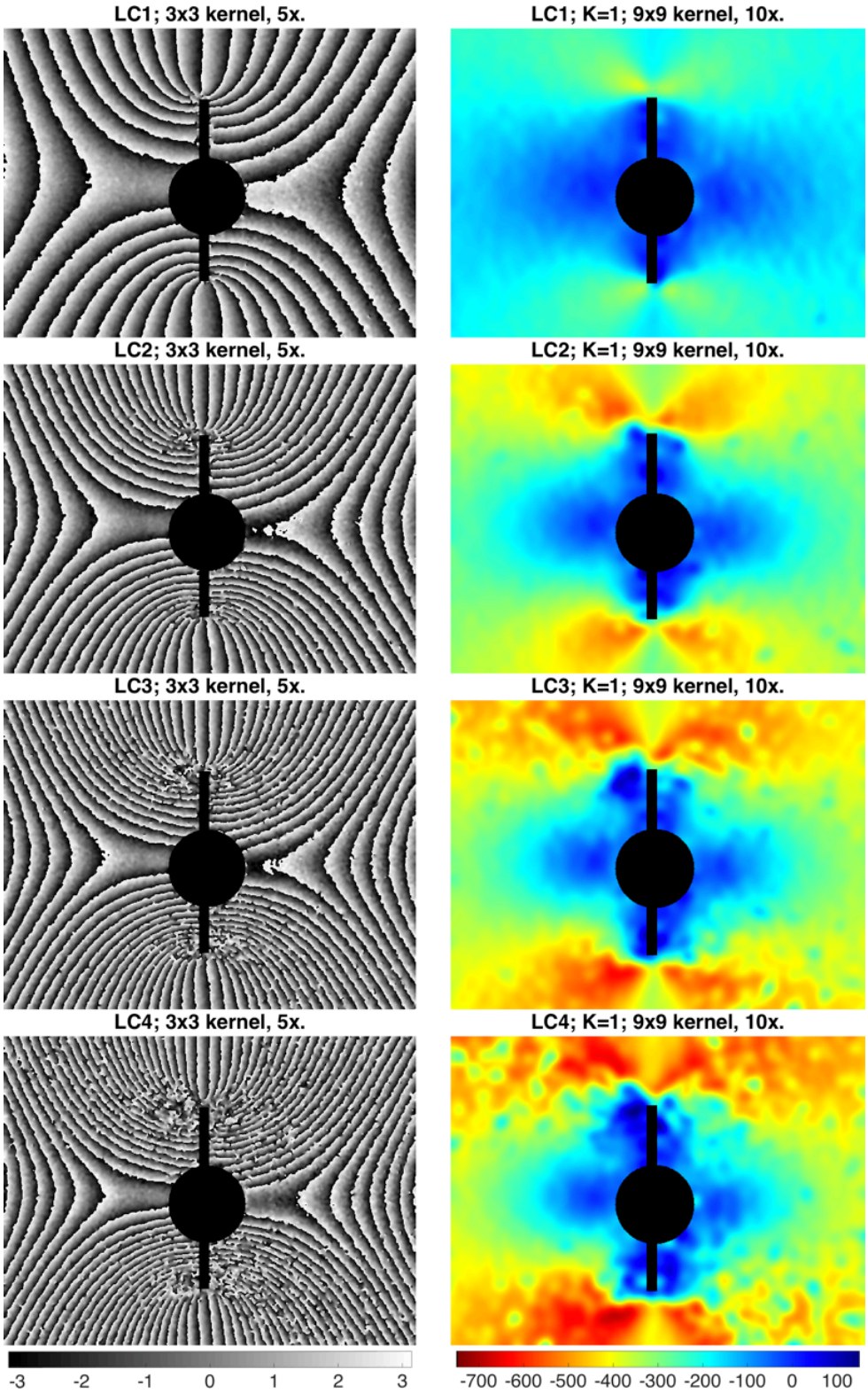

Figure 6.8 *Filtered low-coherence phase patterns (left column) and corresponding calculated strain fields (right column) at different loading levels. The applied compressive loading level increases from top to bottom. Phase is shown in radians and the unit of strain is microstrain (strain x10^{-6}).*

The fringe and strain distributions corresponded very closely to those obtained with the high-coherence setup. The fringes were a bit more symmetric in the low-coherence data, which is likely due to slight tilting of the compression plate axis compared to the high-coherence measurements. Each fringe in the low-coherence data corresponded to 1.2 times larger displacement in comparison with the high-coherence data because of higher wavelength of the laser diode (638 nm vs. 532 nm). At the lowest loading LC1 the overall data quality was very good; no filtering errors were present and the calculated strain field was smooth. When the loading was increased, the findings were in line with the earlier high-coherence results: the level of speckle decorrelation noise increased, ultimately limiting the level of maximum strains that could be resolved. The maximum resolvable compressive strain in the highest loading LC4 was 686 microstrain. In general, however, the low-coherence measurements contained more noise than the high-coherence measurements. At a comparable level of loading the high-coherence setup produced more smooth phase pattern: the fringe contours were less coarse and the overall texture was finer. Consequently, the high-coherence strain maps were also more smooth than those obtained with the low-coherence setup. The factors affecting these differences will be studied in more detail next.

6.5 Measurement quality evaluation

The measurement quality was investigated using visibility maps. The low-coherence data obtained with and without the diffraction grating were compared to the high-coherence data. The corresponding visibility maps are shown in Figure 6.9. The visibility map for the low-coherence data without any path length compensation shows a periodic, varying pattern. By referring to phase and strain maps in Figure 6.7, it can be seen that high visibility was directly correlated with high measurement quality. Adding a diffraction grating to the setup improved overall visibility and made it uniform. This further proves that path length compensation using a diffraction grating is indeed achievable. However, the high-coherence setup had significantly higher visibility than the low-coherence grating setup. A significant light intensity decrease towards the edges of the image explains the apparent visibility variations in the high-coherence setup. The higher visibility leads to higher quality and consequently to lower amount of noise.

The uniform visibility with the diffraction grating indicates that the grating alignment and correspondingly the path length compensation had been performed correctly. The root cause for the different visibilities is likely found from the hardware. The DPSS laser had a commercial current driver optimized for this specific laser. The laser diode, however, was driven with a simple in-house built current source. This driver had no monitoring or active control over the laser diode temperature. Over the course of measurements it was found that if the diode had been on for a very long period of time, the performance could suddenly change. Because temperature is a key performance variable for laser diodes, any temperature drifts or deviations from the optimal operating

temperature directly affect the coherence characteristics and thus the measurement quality. A temperature control circuit could thus help to further improve the performance of the laser diode and the low-coherence setup.

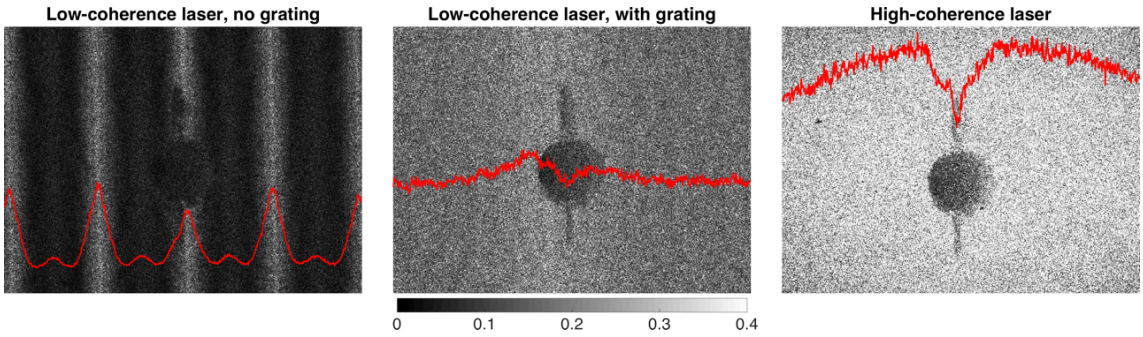

Figure 6.9 *ESPI visibility map comparison. Left: Using a low-coherence laser, Center: Using a low-coherence laser and diffraction grating based path length compensation; Right: Using a high-coherence laser. The red line plots show the column averages of visibility.*

Caution must be used when comparing the quality of filtered synthetic and experimental data. The numerical synthetic noise used was Gaussian, i.e. additive, while real speckle noise is multiplicative. Speckle noise is often approximated as additive [36, 37]. In the case of the repetitive filtering algorithm this approximation is also justifiable, as the mean filtering steps convert the multiplicative speckle noise into additive. While the level of noise was carefully adjusted to be comparable to experimental noise levels, some differences have likely been present. In addition, the distribution of the generated noise was homogeneous, while the real noise distribution was dependent on the magnitude of strains and consequent speckle decorrelation effects. Furthermore, the synthetic strain gradients were set to occur only in the horizontal direction. Consequently, the phase fringes were also oriented symmetrically. The fact that fringe direction corresponded to the direction of the pixel grid, combined with the uniform noise distribution, made the filtering of the synthetic data quite successful even at the very dense areas. However, the synthetic pattern was an important tool for studying and ensuring the validity of the filtering parameters.

In future, the data validation process could be further improved to cover experimental data directly. Using e.g. a four point bent fixture [3], a symmetric object could be uniformly deformed so that it would have even strain distribution. The bending force of the fixture could be directly measured and the expected strain distribution calculated using FEM software. Then, the estimated strain values could be compared to experimental values and potential differences investigated more thoroughly.

6.6 Measurement range considerations

The maximum measurable strain limit can be extended to some extent by altering the measurement setup parameters. According to equation (2.12), decreasing illumination angles or increasing laser wavelength reduces the phase change that occurs for a certain displacement. As a consequence, same level of strain would cause smaller phase gradients and thus a less dense fringe pattern that would be easier to filter. However, these types of changes are limited by geometry and visible spectrum, since small angle geometry and infrared light, respectively, would be impractical to use. In addition, these changes would not increase the dynamic range of the measurement. Instead, the increase in maximum strains would come at a cost of reduced sensitivity. Another option could be to limit the camera field of view, i.e. use larger magnification ratio. This way the phase gradients and physical distances on the object per image pixel would be smaller and consequently larger filtering kernels could be applied while maintaining equal spatial resolution. The downside is that a smaller area of the object would be recorded, directly limiting the maximum size of the measurement objects.

Because the achievable strain range depends on the specific measurement setup parameters, it is more illustrating to investigate the resolvable maximum phase gradients rather than absolute strain values when investigating the performance of ESPI filtering methods. Being able to successfully filter high fringe density data is the key to ultimate performance. Table 1 presents the maximum resolvable strains in each loading HC1–HC4 and LC1–LC4 in both microstrains and phase gradients per pixel.

Table 6.1 *Comparison of highest resolvable strain and phase gradient values in different loadings for the high-coherence and the low-coherence data.*

Measurement series	Loading level	Maximum compressive strain [microstrain]	Maximum phase gradient [rad/pixel]
High-coherence measurements	HC1	340	0.31
	HC2	628	0.58
	HC3	723	0.67
	HC4	744	0.69
Low-coherence measurements	LC1	377	0.35
	LC2	555	0.51
	LC3	627	0.58
	LC4	686	0.64

In the high-coherence data the maximum resolvable phase gradient was 0.69 rad/pixel and close to the level of maximum phase gradient used in the synthetic fringe pattern (0.75 rad/pixel). In the low-coherence data, on the other hand, the maximum resolution was only slightly lower, 0.64 rad/pixel.

6.7 Performance comparison

Modulation amplitude based phasor weighting [21] was considered during the algorithm development. At a single filtering repetition and with small filtering kernels the effectiveness of the phasor weighting was not found to be sufficient. Large kernels, on the other hand, could not be applied to the wrapped data due to high fringe density. When multiple filtering repetitions were used, the effect of the phasor weighting on the end result was found to be negligible. This is likely due to effectiveness of the repetitive filtering scheme. Similar observations were made when studying the effect of gauge length parameter. At a single repetition a longer gauge clearly improved the filtering in areas where wrapping errors were not an issue, but because of small kernel the filtered data still contained high amount of noise. When the number of repetitions was increased, the difference between the different gauge lengths decreased. At five or ten repetitions, a higher gauge had no advantages but the potential wrapping errors still persisted. These findings lead to the use of unit phasor weighting and the smallest gauge length in the central difference strain calculation.

The pixel quality based interpolation method [41] was readily implemented in the Helios program. It was found that at moderate load levels the performance of interpolation was excellent but in the presence of large displacements the areas of highest deformations became corrupted by the interpolation process. As discussed earlier, it is expected that the variation parameter is the bottleneck of the pixel quality based interpolation. Large strains lead to large true variations even within the close neighbourhood of a studied pixel. When combined with high noise level, the number of high variation and thus faulty pixels becomes very large and the interpolation becomes less accurate. Relaxing the variation threshold value or removing the parameter entirely would decrease the number of false negative type errors, but at the same time the quality estimation capability would likely become weaker.

The repetitive strain calculation algorithm took 0.19 seconds to run on a 2 GHz Quad-Core i7 laptop. The time included loading the image frames, then calculating and filtering the phase map using a 3x3 kernel and five repetitions, and finally calculating and filtering the strain map using a 9x9 kernel and 10 repetitions. The written Matlab code was optimized using vectorized inbuilt functions. For example, the use of convolution made a dramatic improvement over an implementation based on nested loops where each pixel in each row in the image data matrix was processed one at a time. An early stage nested loop version of the algorithm took several tens of seconds to run using large kernels and high number of iterations.

In comparison, the TV filtering method developed by Huang et al. took 2.04 seconds to filter a 576x768 pixel shearography image with maximum phase gradient of 0.5 rad/pixel. No statement was made whether this was considered as the resolution limit of their method. The algorithm was implemented in Matlab and run on a 2.8 GHz i7 laptop [36]. Bioucas et al. tested the LPA based phase filtering algorithm using a simulated InSAR satellite radar image and a synthetic Gaussian surface. The Gaussian surface with very dense phase gradients exceeding 2 rad/pixel was successfully filtered. However, the standard deviation of the noise was significantly lower than what was used in in this thesis (0.75 vs. 1.1). The LPA algorithm code was based on Matlab with some parts implemented as C functions and took 30 seconds on a 3.4 GHz Pentium 4 computer to filter a 78x100 pixel image [37]. On the other hand, the pixel quality interpolation in the Fortran-based Helios program took only a fraction of a second to execute using the same data sets as in this thesis. It must be remembered that all these three methods yield an unwrapped phase pattern; their primary goal was not to calculate strain fields. Strain calculation would require additional computation and time, although Huang et al. get the strain field as an intermediate result of the TV-algorithm. Because unwrapping is often the most time-consuming step in strain calculation process, avoiding unwrapping entirely makes the fast processing time of the developed algorithm possible. Time wise, Cloud's method [20] based on local unwrapping and least squares strain calculation could be a contender. However, for sufficient filtering effect the least squares fitting kernel requires very large gauge lengths that severely limit the measurable strain range.

In addition to different goals and different types of data used, exact computation time comparison is challenging for two reasons. First, different algorithms have been implemented using different programming languages and coded by people having different levels of programming experience. Programming languages differ in how they process the code. Matlab is an interpreted language and, in general, slower than compiled languages like C or Fortran. However, Matlab is easy to adopt without earlier programming experience and has a wide range of inbuilt functions for complex computation and graphical presentation, so it suits well the needs of scientific research work. The second complicating factor is the use of different hardware: an average computer today is much more powerful than an average computer ten years ago. For ideal comparison, the different algorithms to be considered should all be fully implemented using the same programming language; written and optimized by the same programmer; and run on the same hardware using the same data. However, this is beyond the scope of this thesis. Regardless, the time comparison presented here illustrates the speed advantage of the developed algorithm and its potential for real time strain imaging.

7. CONCLUSION

Assessing the mechanical strength of materials and components is of crucial importance for ensuring their safety and durability. Because material faults emerge as strain concentrations, strain measurements provide a practical means for quality control. Electronic speckle pattern interferometry (ESPI) is an advanced optical method for measuring the displacement distribution on the surface of a test object. Strain field can be calculated from the displacement data using numerical differentiation. In this thesis, a strain calculation algorithm was developed for resolving high in-plane strain concentrations from ESPI data. As a secondary objective, a novel ESPI setup based on the combination of a low-coherence laser diode and a reflection diffraction grating was developed.

The algorithm is based on handling the data in phasor format and repetitively mean filtering the displacement and strain fields. Phasor format removes the need to unwrap the data prior to strain calculation. This reduces potential errors and significantly speeds up the data processing, since unwrapping is very sensitive to noise and computationally demanding. Because numerical differentiation amplifies noise, the measured displacement data has to be filtered prior to strain calculation. Filtering high strain data is challenging because large deformations cause significant speckle decorrelation noise, reducing the signal SNR. Here, the displacement data is repeatedly mean filtered using a small filtering kernel. Small kernel allows maintaining high spatial resolution. Repeated filtering leads to self-adaptive data correction where the areas most affected by noise are filtered more than areas with less noise. Excessive filtering can, however, cause potential filtering errors to spread and cause data smearing. To prevent this, the number of filtering repetitions has to be limited. As a consequence, some residual noise is left that has to be filtered away from the calculated strain field. Thus, also the strain field is repetitively mean filtered.

Despite its simplicity, the developed algorithm is very effective. However, because it is based on mean filtering, some slight blurring occurs. This is controlled by the adjustment of the filtering parameters. Optimal parameters were studied with both synthetic and experimental displacement data. Five filtering repetitions using a 3x3 pixel kernel were seen as the optimal for displacement fields, and for strain data 9x9 pixel kernel at ten repetitions lead to best results. The exact values understandably depend on the data. The algorithm is straightforward to apply on continuous surfaces. If the region of interest contains discontinuities, they can be masked and thus excluded from the calculations.

Generally, ESPI measurements require high-coherence lasers that tend to be bulky and expensive. Here, a novel ESPI setup based on a low-coherence laser diode and a reflection diffraction grating was developed. The grating compensates the path length differences that normally occur between the interferometer arms. This makes measurements even with low-coherence light possible. ESPI path length compensation using a reflection diffraction grating was demonstrated for the first time. Reflection gratings have much higher light efficiency than previously used transmission gratings.

Experimental measurements were done using the developed novel ESPI setup and compared with the results obtained with traditional high-coherence ESPI. The combination of the low-coherence laser diode and a reflection diffraction grating was successfully shown to yield full field strain measurements with uniform quality. The test specimen used was a compressively loaded rectangular nylon specimen that had a hole and vertical slit patterns. Measurements were done at several loading levels. Larger loads lead to increasing speckle decorrelation effects and consequently to higher noise that ultimately limited the strain range. The maximum resolved strains were 744 microstrain (0.69 rad/pixel) for the high-coherence setup and 686 microstrain (0.64 rad/pixel) for the low-coherence setup. The overall performance of the high-coherence setup was better, which was quantitatively seen as a higher fringe visibility and qualitatively as more smooth data with less filtering errors.

As a low-power and compact system, laser-diode based ESPI would be attractive for field measurements. However, commercial use would require better performance. It is expected that with improved hardware, notably using active diode temperature control, the quality of the low-coherence measurement could be further improved and the gap to high-coherence lasers reduced. Furthermore, by adding a second measurement axis in vertical direction, shear strains and all plane strain components could be measured.

The developed algorithm was implemented in Matlab and took only 0.19 seconds to run. The avoidance of the data unwrapping and low computational complexity were the key factors for achieving such high performance. The high processing speed makes the developed algorithm attractive for live strain monitoring, enabling investigations of dynamic deformation events.

BIBLIOGRAPHY

[1] F. Beer, E. Johnston, J. Dewolf, and D. Mazurek, *Mechanics of Materials*, 6th edition, McGraw-Hill, 2012.

[2] M. Steinzig, and E. Ponslet, "Residual stress measurement using the hole drilling method and laser speckle interferometry: Part II," *Experimental Techniques*, vol 27, no. 4, pp. 17–21, 2003.

[3] G. Schajer, and M. Steinzig "Dual-axis hole-drilling ESPI residual stress measurements," *Journal of Engineering Materials and Technology*, vol. 132, no. 1, pp. 633–642, 2009.

[4] ASTM, "Determining residual stresses by the hole-drilling strain-gage method," ASTM Standard Test Method E837-08, *American Society for Testing and Materials*, West Conshohocken, PA, USA, 2008.

[5] W. Steinchen, and L. Yang, *Digital Shearography: Theory and Application of Digital Speckle Pattern Shearing Interferometry*. SPIE, Bellingham, WA, USA, 2003.

[6] C. Baldwin, "Optical fiber strain gages," in: W. Sharpe (ed), *Springer Handbook of Experimental Solid Mechanics*. Springer, pp. 347–370, 2008.

[7] G. Cloud, "Basics of Optics," in: W. Sharpe (ed), *Springer Handbook of Experimental Solid Mechanics*. Springer, pp. 447–479, 2008.

[8] G. Gülker, K. Hinsch, and A. Kraft, "Deformation monitoring on ancient terracotta warriors by microscopic TV-holography," *Optics and Lasers in Engineering*, vol. 36, no. 5, pp. 501–513, 2001.

[9] D. Albrecht, M. Franchi, A. Lucia, P. Zanetta, A. Aldrovandi, T. Cianfanelli, P. Riitano, O. Sartiani, and D. Emmony, "Diagnostic of the conservation state of antique Italian paintings on panel carried out at the Laboratorio di Restauro dell'Opificio delle Pietre Dure in Florence, Italy with ESPI-based portable instrumentation," *Journal of Cultural Heritage*, vol. 1, no. 1, pp. S331–S335, 2000.

[10] D. Roylance, *Mechanical properties of materials*, Massachusetts Institute of Technology, 2008.

[11] J. Leendertz, "Interferometric displacement measurement on scattering surfaces utilizing speckle effect," *Journal of Physics E: Scientific Instruments*, vol. 3, no. 3, pp. 214–218, 1970.

[12] R. Jones, and C. Wykes, *Holographic and Speckle Interferometry*. 2 ed., Cambridge University Press, Cambridge, UK, 1989.

[13] M. Steinzig, and E. Ponslet, "Residual stress measurement using the hole drilling method and laser speckle interferometry: Part I," *Experimental Techniques*, vol. 27, no. 3 pp. 43–46, 2003.

[14] H. Aebischer, and S. Waldner, "Strain Distributions made visible with image-shearing speckle pattern interferometry," *Optics and Lasers in Engineering*, vol. 26, no. 4–5, pp.407–420, 1997.

[15] Y. Hung, and C. Liang, "Image-shearing camera for direct measurement of surface strains," *Applied Optics*, vol. 18, no. 7, pp. 1046–1051, 1979.

[16] J. Tyrer, and J. Petzing, "In-plane electronic speckle pattern shearing interferometry," *Optics and Lasers in Engineering*, vol. 26, no. 4–5, pp. 395–406, 1997.

[17] D. Denby, and J. Leendertz, "Plane-surface strain examination by speckle-pattern interferometry using electronic processing," *Journal of Strain Analysis*, vol. 9, no. 1, pp. 17-25, 1974.

[18] D. Ghiglia, and M. Pritt, *Two-dimensional phase unwrapping: theory, algorithms, and software*. Wiley, Chichester, UK, 1998.

[19] H. Aebischer, and S. Waldner, "A simple and effective method for filtering speckle-interferometric phase fringe patterns," *Optical Communications*, vol. 162, no. 4–6, pp. 205–210, 1999.

[20] F. Lanza di Scalea, S. Hong, and G. Cloud, "Whole-field strain measurement in a pin-loaded plate by electronic speckle pattern interferometry and the finite element method," *Experimental Mechanics*, vol. 38, no. 1, pp. 55–60, 1998.

[21] B. Ströbel, "Processing of interferometric phase maps as complex-valued phasor images," *Applied Optics*, vol. 35, no. 13, pp. 2192–2198, 1996.

[22] K. Kobayashi, "Single Frequency and Tunable Laser Diodes," *Journal of Lightwave Technology*, vol. 6, no. 11, pp. 1623–1633, 1988.

[23] "Visible Laser Diodes: Center Wavelengths from 404 nm to 690 nm," Thorlabs 2016. [Online]. Available: https://www.thorlabs.com/newgrouppage9.cfm?objectgroup_id=7 [Accessed: 28 March 2016]

[24] M. Viotti, and A. Albertazzi G. Jr, “Industrial inspections by speckle interferometry: General requirements and a case study,” *Optical Measurement Systems for Industrial Inspection VI*, Proc. SPIE Vol. 7389, 15 pages, 2009.

[25] D. Findeis, and J. Gryzagoridis, “Inspecting glassfibre reinforced plastic piping using portable ESPI and shearography,” *Proceedings of the 14th World Conference on NDT*, vol. 14, pp. 1521–1524, 1996.

[26] N. Abramson, S-G Petterson, and H. Bergstrom, “Light-in-flight recording. 5: Theory of slowing down the faster-than-light motion of the light shutter,” *Applied Optics*, vol. 28, no. 4, pp. 759–765, 1989.

[27] G. Schajer, Y. Zhang, and S. Melamed, “In-plane ESPI using an achromatic interferometer with low-coherence laser source,” *Optics and Lasers in Engineering*, vol. 67, pp. 116–121, 2015.

[28] G. Cloud, “Optical Methods in Experimental Mechanics Part 45: Measuring phase difference – Part I: The problem,” *Experimental Techniques*, vol. 35, no. 1, pp. 3–7, 2011.

[29] G. Cloud, “Optical Methods in Experimental Mechanics Part 46: Measuring phase difference – Part II: Compensation,” *Experimental Techniques*, vol. 35, no. 2, pp. 3–6, 2011.

[30] Y. Gan, and W. Steinchen, “Speckle methods,” in: W. Sharpe (ed), *Springer Handbook of Experimental Solid Mechanics*. Springer, pp. 655–673, 2008.

[31] G. Cloud, “Optical Methods in Experimental Mechanics Part 25: Objective speckle,” *Experimental Techniques*, vol. 31, no. 1, pp. 15–17, 2007.

[32] G. Cloud, “Optical Methods in Experimental Mechanics Part 26: Subjective speckle,” *Experimental Techniques*, vol. 31, no. 2, pp. 17–19, 2007.

[33] G. Cloud, “Optical Methods in Experimental Mechanics Part 27: Speckle size estimates ,” *Experimental Techniques*, vol. 31, no. 3, pp. 19–22, 2007.

[34] R. Goldstein, H. Zebker, and C. Werner, “Satellite radar interferometry: Two-dimensional phase unwrapping,” *Radio Science*, vol. 23, no. 4, pp. 713–720, 1988.

[35] S. Chavez, Q-S. Xiang, and L. An, “Understanding phase maps in MRI: A new cutline phase unwrapping method,” IEEE Transactions on Medical Imaging, vol. 21, no. 8, pp. 966–977, 2002.

[36] H. Huang, L. Tian, Z. Zhang, Y. Liu, Z. Chen, and G. Barbastathis, "Path-independent phase unwrapping using phase gradient and total-variation (TV) denoising," *Optics Express*, vol. 20, no. 13, pp. 14075–14089, 2012.

[37] J. Bioucas-Dias, V. Katkovnik, J. Astola, and K. Egiazarin, "Absolute phase estimation: adaptive local denoising and global unwrapping," *Applied Optics*, vol. 47, no. 29, pp. 5358–5369, 2008.

[38] H. Vrooman, and A. Maas, "Image processing algorithms for the analysis of phase-shifted speckle interference patterns," *Applied Optics*, vol. 30, no. 13, pp. 1636–1641, 1991.

[39] W. Osten, "Digital image processing for optical metrology," in: W. Sharpe (ed), *Springer Handbook of Experimental Solid Mechanics*. Springer, pp. 481–563, 2008.

[40] N. Mohan, "Speckle methods and applications," in: T. Yoshizawa (ed), *Handbook of Optical Metrology – Principles and Applications*. CRC Press, pp. 241–271, 2009.

[41] Y. An, and G. Schajer, "Pixel quality evaluation and correction procedures in ESPI," *Proceedings of the SEM Annual Conference*, 7 pages, 2009.

[42] J. Bioucas-Dias, and M. Figueiredo, "Multiplicative noise removal using variable splitting and constrained optimization," *IEEE Transactions on Image Processing*, vol. 19, no. 7, pp. 1720–1730, 2010.

[43] M. Servin, J. Estrada, J. Quiroga, J. Mosiño, and M. Cywiak, "Noise in phase shifting interferometry," vol. 17, no. 11, pp. 8789–8794, 2009.

[44] R. Haglund, "The properties of light," in: F. Träger (ed), *Springer Handbook of Lasers and Optics*. Springer, pp. 4–34, 2012.

[45] O. Svelto, *Principles of Lasers*, 5th edition, Springer, 2010.

[46] E. Hecht, *Optics*, 4th edition, Addison Wesley, 2003.

[47] C. Akcay, P. Parrein, and J. Rolland, "Estimation of longitudinal resolution in optical coherence imaging," *Applied Optics*, vol. 41, no. 25, pp. 5256–5262, 2002.

[48] C. Palmer, *Diffraction Grating Handbook*, 5th edition, Thermo RGL, 2002.

[49] M. Viotti, W. Kapp, and A. Albertazzi Jr., "Achromatic digital speckle pattern interferometer with constant radial in-plane sensitivity by using a diffractive optical element," *Applied Optics*, vol. 48, no. 12, pp. 2275–2281, 2009.

[50] "Introduction to diffraction grating," Thorlabs. [Online]. Available: https://www.thorlabs.com/catalogpages/805.pdf [Accessed: 23 December 2015].

[51] Samuel Melamed, "Compact ESPI device for isotropic measurements of residual stress," *University of British Columbia*, Vancouver, Master of Science thesis, 103 pages, 2015.

[52] "Visible Ruled Reflective Diffraction Gratings," Thorlabs 2016. [Online]. Available: http://www.thorlabs.de/newgrouppage9.cfm?objectgroup_id=8626 [Accessed: 12 June 2016].

[53] "Visible Transmission Gratings," Thorlabs 2016. [Online]. Available: http://www.thorlabs.de/newgrouppage9.cfm?objectgroup_id=1123 [Accessed: 12 June 2016].